



Energy transfers between multidecadal and turbulent variability

Antoine Hochet, Thierry Huck, Olivier Arzel, Florian Sévellec, Alain Colin de Verdière

► To cite this version:

Antoine Hochet, Thierry Huck, Olivier Arzel, Florian Sévellec, Alain Colin de Verdière. Energy transfers between multidecadal and turbulent variability. *Journal of Climate*, inPress, 35 (4), pp.1157-1178. 10.1175/JCLI-D-21-0136.1 . hal-03390256

HAL Id: hal-03390256

<https://hal.science/hal-03390256>

Submitted on 21 Oct 2021

HAL is a multi-disciplinary open access archive for the deposit and dissemination of scientific research documents, whether they are published or not. The documents may come from teaching and research institutions in France or abroad, or from public or private research centers.

L'archive ouverte pluridisciplinaire **HAL**, est destinée au dépôt et à la diffusion de documents scientifiques de niveau recherche, publiés ou non, émanant des établissements d'enseignement et de recherche français ou étrangers, des laboratoires publics ou privés.

Energy transfers between multidecadal and turbulent variability

Antoine Hochet^{*}, Thierry Huck, Olivier Arzel, Florian Sévellec, and Alain Colin de Verdière

Univ Brest, CNRS, Ifremer, IRD, Laboratoire d'Océanographie Physique et Spatiale (LOPS,

UMR 6523), IUEM, Brest, France

^{*}*Corresponding author address:* Antoine Hochet, Univ of Brest, CNRS, Ifremer, IRD, Laboratoire

d'Océanographie Physique et Spatiale (LOPS, UMR 6523), IUEM, Brest, France

E-mail: antoine.hochet@univ-brest.fr

ABSTRACT

8 One of the proposed mechanisms to explain the multidecadal variability ob-
9 served in sea surface temperature of the North Atlantic consists of a large-
10 scale low-frequency internal mode spontaneously developing because of the
11 large-scale baroclinic instability of the time-mean circulation. Even though
12 this mode has been extensively studied in terms of the buoyancy variance bud-
13 get, its energetic properties remain poorly known. Here we perform the full
14 mechanical energy budget including available potential energy (APE) and ki-
15 netic energy (KE) of this internal mode and decompose the budget into three
16 frequency bands: mean, low frequency (LF) associated with the large-scale
17 mode and high frequency (HF) associated with mesoscale eddy turbulence.
18 This decomposition allows us to diagnose the energy fluxes between the dif-
19 ferent reservoirs and to understand the sources and sinks. Due to the large-
20 scale of the mode, most of its energy is contained in the APE. In our configu-
21 ration, the only source of LF APE is the transfer from mean APE to LF APE
22 that is attributed to the large-scale baroclinic instability. In return the sinks
23 of LF APE are the parameterized diffusion, the flux toward HF APE and to a
24 much lesser extent toward LF KE. The presence of an additional wind-stress
25 component weakens multidecadal oscillations and modifies the energy fluxes
26 between the different energy reservoirs. The KE transfer appears to only have
27 a minor influence on the multidecadal mode compared to the other energy
28 sources involving APE, in all experiments. These results highlight the utility
29 of the full APE/ KE budget.

30 **1. Introduction**

31 The multidecadal large-scale variability of the Sea Surface Temperature (SST) is characterised
32 in the North Atlantic by an anomaly intensified in the subpolar region and by a weaker anomaly
33 of opposite sign south of the equator (Kushnir 1994; Deser et al. 2010; Zhang et al. 2019). This
34 large scale SST variability has been named Atlantic Multidecadal Variability (AMV, Kushnir 1994;
35 Schlesinger and Ramankutty 1994; Kerr 2000; Sutton et al. 2018). Cool AMV phases occurred
36 in the 1900s-1920s, 1960s-1990s and warm phases occurred in the 1930s-1960s and after 1995.
37 These cool and warm phases have been shown to be associated with several regional climate
38 impacts such as the Sahel Indian summer monsoon rainfall, Atlantic hurricanes frequency, summer
39 climate over western Europe and north America (Zhang et al. 2019), wave climate in the Atlantic
40 and Pacific Ocean (Reguero et al. 2019). Observations moreover show that more heat is released
41 from the North Atlantic ocean to the atmosphere during a positive phase of the AMV (Gulev
42 et al. 2013). Thus understanding what controls the dynamics of this variability and its potential
43 predictability have essential societal and economics implications (Sutton et al. 2018).

44 Several mechanisms have been proposed to explain the origin of the AMV and remain actively
45 debated (see for instance the recent discussion in Clement et al. 2015; Zhang et al. 2016; Clement
46 et al. 2016). Some studies suggest a direct role of the atmosphere either via stochastic heat flux
47 (Hasselmann 1976; Frankignoul and Hasselmann 1977; Clement et al. 2015) or via aerosol emis-
48 sions (Booth et al. 2012), while other studies (e.g. Sévellec and Fedorov 2013; Arzel et al. 2018)
49 suggest a role for oceanic processes linked with the internal variability of the Atlantic Merid-
50 ional Overturning Circulation (AMOC). In this work we focus on improving our knowledge of the
51 physics of internal ocean modes which are one of the possible explanations for the AMV. At low
52 resolution, internal interdecadal variability arises in rectangular flat bottomed single hemispheric

53 basin forced by prescribed surface heat fluxes (Greatbatch and Zhang 1995; Huck et al. 1999). This
54 internal variability is due to a large-scale baroclinic instability that gives rise to SST anomalies and
55 to geostrophically-induced Meridional Overturning Circulation variability (Colin de Verdière and
56 Huck 1999; Te Raa and Dijkstra 2002). This mode of variability and its mechanism were also
57 demonstrated to exist in global realistic configuration of an Ocean General Circulation Model
58 (OGCM) (Sévellec and Fedorov 2013), in idealized coupled models (Buckley et al. 2012; Jamet
59 et al. 2016), in climate models (Muir and Fedorov 2017) and in observations (Frankcombe et al.
60 2008). It is also shown to produce maximum SST variance in the region where the AMV signature
61 is observed (Arzel et al. 2018).

62 The mode can be damped in some models (such as in the study of Sévellec and Fedorov (2013))
63 and self-sustained in others (Huck et al. (2015) for instance). The damped or self-sustained na-
64 ture of the mode depends on different parameters such as the topography (Winton 1997), the
65 wind shape and strength, or the vertical and horizontal diffusion (Huck et al. 2001; Arzel et al.
66 2018). In the case of a damped mode, atmospheric stochastic forcing is needed to excite the
67 mode. Frankcombe et al. (2009) showed that the introduction of a North Atlantic Oscillation type
68 stochastic forcing leads to an amplitude of sea surface temperature variability comparable to obser-
69 vations. Arzel et al. (2018) studied the bifurcation structure of the mode in a realistic configuration
70 forced by prescribed surface fluxes and showed that the mode becomes damped for eddy induced
71 diffusivities larger than 600 m s^{-1} .

72 In addition to available potential energy fluxes associated with the large-scale instability mech-
73 anism, ocean mesoscales eddies have been shown to be at the origin of a spatio-temporal inverse
74 cascade of kinetic energy (Arbic et al. 2014; Martin et al. 2020). This latter mechanism has been
75 proposed to be central to the existence of interannual-to-decadal fluctuations of sea level anoma-
76 lies and surface kinetic energy in global-scale eddy simulations (Penduff et al. 2011; Arbic

et al. 2014; Sérazin et al. 2015, 2018; Martin et al. 2020) and to influence the AMOC variability
 (Grégorio et al. 2015; Leroux et al. 2018; Jamet et al. 2019). However, realistic and global-
 scale eddy resolving simulations of multidecadal variability are still beyond reach because of the
 long-time integration required to bring the circulation in near equilibrium with the weak interior
 diffusive vertical fluxes. Therefore most of the studies devoted to this problem are based on simple
 box-model geometries (e.g., Spall 2008; Huck et al. 2015; Hochet et al. 2020). How the oceanic
 mesoscale turbulence influences the multidecadal mode that spontaneously develops under pre-
 scribed surface fluxes has been explored by Huck et al. (2015). These authors show that, in the
 presence of mesoscale turbulence, the primary mechanism driving multidecadal-scale temperature
 fluctuations remains the large-scale baroclinic instability mechanism. The presence of a surface
 restoring boundary condition in Spall (2008) prevents the internal ocean mode from developing so
 that the wind-driven gyre circulation and subsequent mesoscale instabilities play a major role. The
 coexistence of the mode described above and mesoscale eddies was shown by Huck et al. (2015)
 using idealized simulations at eddy-resolving resolution. In such eddying configurations and us-
 ing a frequency-domain approach, Hochet et al. (2020) have highlighted a non-linear transfer of
 temperature variance from low to high frequencies: mesoscale eddies are a sink of temperature
 variance for the low frequency mode. Hence low-frequencies do not arise as the result of the
 mesoscale eddy field, as in Spall (2008) for instance, but instead draw their energy source from
 the large-scale stratification. Sévellec et al. (2020) have also shown a similar behavior using moor-
 ing data in the Southern Ocean, but on shorter timescale. However the use of temperature variance
 instead of an energetic framework, as in Arbic et al. (2014) or Sérazin et al. (2015, 2018) makes
 the comparison with results from these studies difficult. Temperature variance is up to a factor
 equal to the local definition of available potential energy (APE) ϵ_{APE} in a Quasi-Geostrophic (QG)

100 framework:

$$\varepsilon_{APE} \approx \frac{1}{2} \frac{g^2 \rho'^2}{\rho_0 N^2} \quad (1)$$

101 with N the Brunt-Väisälä frequency, g the acceleration of gravity parameter, ρ' the density
102 anomaly and ρ_0 the reference density. However, the internal mode described in the literature
103 cited above occurs in regions where isopycnals outcropping prevents the use of (1). Thus diagnos-
104 tics and budget of temperature variance do not permit identifying the sources and sinks of energy.
105 In this article we seek to obtain the full energy budget (i.e., including both kinetic energy (KE)
106 and available potential energy) for the low frequency mode described for instance in Hochet et al.
107 (2020) and to quantify the energy transfers associated with the time mean flow and mesoscale eddy
108 field. In particular we want to compare the intensity and direction of the conversion between Low
109 Frequency (LF) and High Frequency (HF) KE and between LF and HF APE. Because the only
110 source of KE in the buoyancy forced experiment of Hochet et al. (2020) is the APE/KE conversion
111 terms, we also investigate the effect of a wind stress forcing to add a direct source of KE.

112 The main difficulty in obtaining the energy budget in different frequency bands lies in the APE
113 decomposition. Indeed, contrary to the kinetic energy, the time decomposition of the full APE
114 formula is not straightforward. Scotti and White (2014) circumvented this problem by computing
115 the fluctuating APE as the difference between the APE for the total circulation (i.e., time mean and
116 fluctuations) and the APE for the time mean circulation. This idea has been applied by Zemskova
117 et al. (2015) to an eddy permitting ocean state estimate (from the “Estimating the Circulation and
118 Climate of the Ocean”, Phase II) to decompose the APE and KE budget into time mean and fluc-
119 tuating components. More recently, the same method has been used by Zemskova et al. (2021)
120 to study the influence of several wind intensities over the Southern Ocean on the time mean and
121 fluctuating components of the APE and KE budget. They found that the APE budget is not signif-
122 icantly affected by the surface wind stress and mainly controlled by the surface buoyancy forcing.

123 However we will show that applying this method to our configuration leads to a spurious imprint
 124 of the time-independent surface heat flux forcing on the LF and HF APE reservoirs, whereas we
 125 would instead expect the energy flux associated with the steady forcing to be entirely imparted
 126 to the background stratification. We will thus develop an alternative method that will be used to
 127 decompose the APE into mean, low frequency, and high frequency parts.

128 The article is organised as follows: in section 2, we decompose the mean, low- and high-
 129 frequencies and derive the budget for APE and KE. In section 3, we give a description of the
 130 model configuration used in this study. In section 4, we describe the variability in three numeri-
 131 cal simulations with idealized North Atlantic configuration and under prescribed surface heat flux
 132 forcing with different wind forcing intensities. In Section 5, we apply the energy budgets described
 133 in section 2 on the simulation outputs. In section 6, we conclude and discuss the main findings.

134 2. Theory

135 In this section we derive the APE and KE budgets for the mean, LF and HF circulations. We use
 136 a linear equation of state for the density ρ that is only a function of temperature: $\rho = \rho_0(1 - \alpha\theta)$
 137 where θ is the temperature, $\alpha = 2 \times 10^{-4} \text{ K}^{-1}$ the uniform thermal expansion coefficient and
 138 $\rho_0 = 1027.5 \text{ kg m}^{-3}$ the reference density (consistently with the ocean model used, see section 3
 139 for the full model description). The equation for ρ is then:

$$\frac{\partial \rho}{\partial t} + \mathbf{v} \cdot \nabla \rho = D + F, \quad (2)$$

140 where $\mathbf{v} = (u, v, w)$ is the 3d velocity with u , v , w the zonal, meridional, and vertical velocities.
 141 D and F represent the dissipation and surface forcing of density, respectively, the latter being
 142 constant with time and zero below the surface (i.e. no penetrative radiation). The time independent
 143 forcing is used here to keep the problem simple, we therefore do not account for slow variation

144 of the forcing linked for instance with climate change. Note that the generalization of the theory
 145 presented below to a time dependent F and to penetrative radiation is straightforward.

146 To obtain a separate budget for the low and high frequency parts of the APE and KE we decom-
 147 pose each field M into mean, low and high frequency parts:

$$M = \overline{M} + M^{\text{LF}} + M^{\text{HF}}, \quad (3)$$

148 where M^{LF} and M^{HF} are the low and high frequency parts of M , respectively, and \overline{M} the time
 149 mean. The time mean is computed using the following formula:

$$\overline{M} = \frac{1}{T} \int_T M dt \quad (4)$$

150 where T is the time length over which the integral is computed so that: M^{LF} and M^{HF} satisfy
 151 $\overline{M^{\text{HF}}} = \overline{M^{\text{LF}}} = \overline{M^{\text{LF}} M^{\text{HF}}} = 0$. To decompose into HF and LF we use a low pass Butterworth filter
 152 (cut-off frequency given in the following section). The low-pass filter is represented by $\widetilde{\cdot}$ so that
 153 M^{HF} satisfies $\widetilde{M^{\text{HF}}} = 0$ and $\widetilde{M} = \overline{M} + M^{\text{LF}}$.

154 Using this decomposition in frequency bands on Eq. (2) gives the following evolution equations
 155 for the mean, LF and HF of ρ :

$$\frac{\partial \overline{\rho}}{\partial t} = -\overline{\mathbf{v}} \cdot \nabla \overline{\rho} - \overline{\mathbf{v}^{\text{LF}} \cdot \nabla \rho^{\text{LF}}} - \overline{\mathbf{v}^{\text{HF}} \cdot \nabla \rho^{\text{HF}}} + \overline{D} + F \quad (5)$$

$$\frac{\partial \rho^{\text{LF}}}{\partial t} = -\overline{\mathbf{v}} \cdot \nabla \rho^{\text{LF}} - \mathbf{v}^{\text{LF}} \cdot \nabla (\overline{\rho} + \rho^{\text{LF}}) + \overline{\mathbf{v}^{\text{HF}} \cdot \nabla \rho^{\text{HF}}} - \mathbf{v}^{\text{HF}} \cdot \widetilde{\nabla \rho^{\text{HF}}} + \overline{\mathbf{v}^{\text{LF}} \cdot \nabla \rho^{\text{LF}}} + D^{\text{LF}} \quad (6)$$

$$\frac{\partial \rho^{\text{HF}}}{\partial t} = -\overline{\mathbf{v}} \cdot \nabla \rho^{\text{HF}} - \mathbf{v}^{\text{LF}} \cdot \nabla \rho^{\text{HF}} - \mathbf{v}^{\text{HF}} \cdot \nabla (\overline{\rho} + \rho^{\text{LF}} + \rho^{\text{HF}}) + \mathbf{v}^{\text{HF}} \cdot \widetilde{\nabla \rho^{\text{HF}}} + D^{\text{HF}} \quad (7)$$

158 APE is obtained as the difference between Potential Energy (PE) and Background Potential Energy
 159 (BPE). We derive expressions for PE, BPE, and APE in sections a, b and c below.

160 *a. Potential Energy*

161 Multiplying Eq. (5) by zg gives an equation for the mean PE :

$$\frac{\partial gz\bar{\rho}}{\partial t} = -\nabla \cdot (g\bar{\mathbf{v}}z\bar{\rho}) + g\bar{w}\bar{\rho} + \overline{g w^{HF} \rho^{HF}} + \overline{g w^{LF} \rho^{LF}} - \nabla \cdot \left(gz(\bar{\mathbf{v}}^{HF} \rho^{HF} + \bar{\mathbf{v}}^{LF} \rho^{LF}) \right) + gz\bar{D} + gz\bar{F}, \quad (8)$$

162 Integrating Eq. (8) on the volume V of the basin and time averaging results in the following
163 equation:

$$\frac{dPE^{MEAN}}{dt} = \underbrace{\int_V g\bar{w}\bar{\rho} dV}_{-C(PE^{MEAN}, KE^{MEAN})} + \underbrace{\int_V g\overline{w^{LF} \rho^{LF}} dV}_{-C(PE^{MEAN}, PE^{LF})} + \underbrace{\int_V g\overline{w^{HF} \rho^{HF}} dV}_{-C(PE^{MEAN}, PE^{HF})} + \underbrace{\int_V gz\bar{D} dV}_{D_{PE}}, \quad (9)$$

164 Note that the volume integral of the forcing term multiplied by z disappears because $z = 0$ at
165 the surface and \bar{F} is zero below the surface. We note $C(A, B)$ the conversion term from A to B
166 with $C(A, B) = -C(B, A)$, if $C(A, B) > 0$ then $C(A, B)$ acts to increase B i. $C(PE^{MEAN}, KE^{MEAN})$,
167 $C(PE^{MEAN}, PE^{LF})$ and $C(PE^{MEAN}, PE^{HF})$ are respectively the conversion of mean PE to mean
168 KE , of mean PE to LF PE and of mean PE to HF PE . D_{PE} is interpreted as the rate of con-
169 version of internal energy to potential energy (e.g. Hughes et al. 2009). There is no potential
170 energy in anomalies because $\overline{gz\rho^{LF}} = \overline{gz\rho^{HF}} = 0$, therefore $PE^{LF} = PE^{HF} = 0$. However, fol-
171 lowing Zemskova et al. (2015), we attribute the two terms $\int_V g\overline{w^{HF} \rho^{HF}} dV$ and $\int_V g\overline{w^{LF} \rho^{LF}} dV$ to
172 $C(PE^{MEAN}, PE^{HF})$ and $C(PE^{MEAN}, PE^{LF})$ so that the formal budgets for PE^{LF} and PE^{HF} are:

$$\frac{dPE^{LF}}{dt} = -C(PE^{LF}, KE^{LF}) + C(PE^{MEAN}, PE^{LF}) \quad (10)$$

173 and:

$$\frac{dPE^{HF}}{dt} = -C(PE^{HF}, KE^{HF}) + C(PE^{MEAN}, PE^{HF}) \quad (11)$$

174 From which we deduce that: $C(PE^{HF}, KE^{HF}) = C(PE^{MEAN}, PE^{HF})$ and $C(PE^{LF}, KE^{LF}) =$
175 $C(PE^{MEAN}, PE^{LF})$.

176 *b. Background Potential Energy*

177 To obtain an equation for the BPE, we first define the reference level $z_r(\rho, t)$ which is a function
 178 of time and density and corresponds to the depth that ρ would have in the Lorenz state of minimum
 179 potential energy (Lorenz 1955), a state where isopycnal surfaces would be horizontal. Following
 180 Saenz et al. (2015), a simple relationship between ρ and its reference level z_r can be derived using
 181 the result that an adiabatic rearrangement of the fluid parcels conserves the volume:

$$\int_{V(\rho, t)} dV = \int_{z_r}^0 A(z_r) dz_r, \quad (12)$$

182 where $V(\rho, t)$ is the volume of water parcels with density ρ' lower than ρ at time t , $A(z)$ is the
 183 area of the ocean at depth z . With a non-linear equation of state for density that depends on
 184 temperature, salinity and pressure, the procedure to obtain z_r is quite complex and described for
 185 instance in Saenz et al. (2015). However, in this work we use two assumptions that greatly simplify
 186 the calculation of z_r . The first is the assumption of a linear equation of state depending only
 187 on temperature. This implies that z_r is a function of density ρ (which is itself a function of
 188 temperature: $\rho = \rho_0(1 - \alpha\theta)$) and time t : $z_r = Z_r(\rho, t)$. The second assumption is the flat bottom
 189 basin with vertical boundaries so that the basin area is independant of depth, i.e. $A(z) = A$. Using
 190 Eq. (12), z_r is then simply:

$$z_r(\rho, t) = -\frac{V(\rho, t)}{A}, \quad (13)$$

191 Note that with a depth dependent ocean area, the reference depth can easily be obtained by solving
 192 Eq. (12). A schematic illustrating how the reference depth $z_r(\rho, t)$ is obtained using volume $V(\rho)$
 193 is shown in Figure 1. This reference depth can be used to rewrite the density ρ as a function of
 194 z_r such that: $\rho(X, t) = \rho_r(Z_r(X, t), t)$, with $Z_r(X, t) = z_r(\rho(X, t), t)$. On this schematic and in this
 195 article, we call “physical space” the usual space described by $X = (x, y, z)$ and t , and the “reference
 196 space” the space described by the reference depth z_r and t .

Figure 2 shows the reference depth z_r as a function of time for different values of temperature from a simulation that will be presented in a following section. The time variation of the function $z_r(\rho, t)$ cannot be neglected here because it varies by more than 500 m for the largest densities due to the presence of the large-scale, low-frequency, mode. In Zemskova et al. (2015) z_r variations with time are small because their study is not focused on the same timescale as ours: their time mean is computed over 20 years and their temporal variability is made of inter-annual, seasonal and shorter timescales while our focus is on decadal to multi-decadal timescales. Note that the larger variations of reference depth at larger densities can be attributed to the stronger (weaker) ρ_r gradient at shallower (deeper) reference depth. Time variation of the reference depths due to seasonal variation and to the presence of eddies was also reported in Zemskova et al. (2015).

The background potential energy is defined as follows:

$$BPE = \int_V gZ_r(X, t)\rho(X, t)dV = \int_{-H}^0 Agz'_r\rho_r(z'_r, t)dz'_r, \quad (14)$$

where H is the basin depth (so that $AH = V$) and where the last equality is obtained from equation (12) and describes the calculation of the BPE in the reference space. We now want to obtain separate budgets for the mean, LF, and HF BPE. In Zemskova et al. (2015) the BPE budget is computed by first calculating the BPE of the mean flow that they define as:

$$BPE_Z^{\text{MEAN}} = \int_V g\bar{\rho}z_r(\bar{\rho})dV, \quad (15)$$

where z_r is the reference depth associated with $\bar{\rho}$. The BPE of anomalies is then defined as the difference between the total BPE and the mean BPE:

$$BPE_Z^{\text{anomalies}} = \int_V \left(g\overline{\rho z_r(\rho, t)} - g\bar{\rho}z_r(\bar{\rho}) \right) dV, \quad (16)$$

214 Using this method in our simulation leads to part of the time independent heat flux forcing being
 215 attributed to $BPE_Z^{anomalies}$. Indeed, in this framework, the BPE forcing by heat fluxes is:

$$\int_V g \bar{F} \left(\overline{z_r(\rho, t)} - z_r(\bar{\rho}) \right) dV, \quad (17)$$

216 where \bar{F} is the time-independent net heat flux at the surface. Because of the non-linearity of the z_r
 217 function (and its time dependence) we have that:

$$\frac{z_r(\rho_1) + z_r(\rho_2)}{2} \neq z_r\left(\frac{\rho_1 + \rho_2}{2}\right), \quad (18)$$

218 for two different densities $\rho_1 \neq \rho_2$. Thus the term in Eq. (17) is non-zero and the time independent
 219 forcing acts on the anomalies. However an analysis in terms of density variance shows that the
 220 time independent heat flux only acts on time mean density (Hochet et al. 2020). Density anomalies
 221 are found to be forced only by the term $\bar{\rho}' \mathbf{u}' \cdot \nabla \bar{\rho}$ which is usually interpreted as the signature of a
 222 large-scale baroclinic instability (see Colin de Verdière and Huck 1999). The fact that the term in
 223 Eq. (17) is non-zero is thus at odds with this interpretation.

224 To circumvent this problem we develop below an alternative method to separate the BPE in
 225 frequency bands. The readers not interested in the details of the BPE decomposition may skip this
 226 section and refer to figure 3 which gives an intuitive view of the transfer between the different
 227 reservoirs.

228 As in the previous section, ρ is first decomposed into three frequency bands: mean, low-
 229 frequency, and high frequency so that:

$$\rho = \bar{\rho} + \rho^{LF} + \rho^{HF}, \quad (19)$$

230 $\rho(X, t) = \rho_r(z_r, t)$ can trivially be written as:

$$\rho(z_r, t) = -\frac{1}{A} \frac{\partial}{\partial z_r} \int_{V(z_r)} \rho(X, t) dV, \quad (20)$$

where $V(z_r)$ is the volume of water with $z'_r > z_r$. This formula simply states that the average of ρ on z_r surfaces is ρ by definition of $z_r(\rho, t)$. Using Eq. (19) in Eq. (20) gives:

$$\rho = -\underbrace{\frac{1}{A} \frac{\partial}{\partial z_r} \int_{V(z_r)} \bar{\rho} dV}_{\rho_r^{MEAN}(z_r, t)} - \underbrace{\frac{1}{A} \frac{\partial}{\partial z_r} \int_{V(z_r)} \rho^{LF} dV}_{\rho_r^{LF}(z_r, t)} - \underbrace{\frac{1}{A} \frac{\partial}{\partial z_r} \int_{V(z_r)} \rho^{HF} dV}_{\rho_r^{HF}(z_r, t)} \quad (21)$$

where ρ_r^{MEAN} , ρ_r^{LF} , and ρ_r^{HF} are the average of ρ^{MEAN} , ρ^{LF} and ρ^{HF} , respectively, on z_r surfaces. This ensures that ρ_r^{MEAN} , ρ_r^{LF} and ρ_r^{HF} are functions of z_r (and time) and this property will be useful to obtain an evolution equation for the BPE as will become clear below. The BPE is then decomposed as follows:

$$BPE = \int_V \overline{\rho g z_r(\rho, t)} dV = \underbrace{\int_V \overline{\rho_r^{MEAN}(z_r, t) g z_r(\rho, t)} dV}_{BPE^{MEAN}} + \underbrace{\int_V \overline{\rho_r^{LF}(z_r, t) g z_r(\rho, t)} dV}_{BPE^{LF}} + \underbrace{\int_V \overline{\rho_r^{HF}(z_r, t) g z_r(\rho, t)} dV}_{BPE^{HF}}, \quad (22)$$

where BPE^{MEAN} , BPE^{LF} , and BPE^{HF} are respectively the BPE associated with the mean, LF and HF densities. The time evolution of the BPE is then the sum of the time evolution of the MEAN, LF, and HF BPE:

$$\frac{dBPE}{dt} = \frac{dBPE^{MEAN}}{dt} + \frac{dBPE^{LF}}{dt} + \frac{dBPE^{HF}}{dt}, \quad (23)$$

The evolution equation for the mean, LF or HF, BPE is:

$$\frac{dBPE^*}{dt} = \int_V g \frac{\partial \rho_r^*}{\partial t} z_r dV + \underbrace{\int_V g \rho_r^* \frac{\partial z_r}{\partial t} dV}_{=0}, \quad (24)$$

where * represents either MEAN, LF, or HF. The second term of the r.h.s. is zero as shown in Winters et al. (1995) and later in Tailleux (2009) because ρ_r^* is constant on z_r surfaces by construction (see Eq. (21)).

The three evolution equations for the mean, LF, and HF density (i.e., Eqs. (5), (6) and (7)) are

averaged on z_r surfaces using the following formula:

$$\frac{\partial \rho_r^*}{\partial t}(z_r, t) = \frac{1}{A} \frac{\partial}{\partial z_r} \left(\int_{V(z_r)} \frac{\partial \rho^*}{\partial t} dV \right), \quad (25)$$

where * represents the mean, LF, or HF density. Using Eq (25) with Eqs (5), (6), and (7), and

inserting in formula (24) leads to the following relations for the three BPE budgets:

$$\frac{dBPE^{MEAN}}{dt} = -C(BPE^{MEAN}, BPE^{LF}) - C(BPE^{MEAN}, BPE^{HF}) + F_{BPE^{MEAN}} + D_{BPE^{MEAN}}, \quad (26)$$

$$\frac{dBPE^{LF}}{dt} = -C(BPE^{LF}, BPE^{HF}) + C(BPE^{MEAN}, BPE^{LF}) + D_{BPE^{LF}}, \quad (27)$$

$$\frac{dBPE^{HF}}{dt} = C(BPE^{LF}, BPE^{HF}) + C(BPE^{MEAN}, BPE^{HF}) + D_{BPE^{HF}}, \quad (28)$$

where the conversion terms are:

$$C(BPE^{LF}, BPE^{HF}) = g \int_V \overline{z_r(\rho, t) \left(\widetilde{\mathbf{v}^{HF} \cdot \nabla \rho^{HF}} - \overline{\mathbf{v}^{HF} \cdot \nabla \rho^{HF}} \right)} - \overline{z_r(\rho, t) \mathbf{v}^{LF} \cdot \nabla \rho^{HF}} dV, \quad (29)$$

$$C(BPE^{MEAN}, BPE^{LF}) = g \int_V \overline{z_r(\rho, t) \mathbf{v}^{LF} \cdot \nabla \rho^{LF}} - \overline{z_r(\rho, t) \bar{\mathbf{v}} \cdot \nabla \rho^{LF}} dV, \quad (30)$$

$$C(BPE^{MEAN}, BPE^{HF}) = g \int_V \overline{z_r(\rho, t) \mathbf{v}^{HF} \cdot \nabla \rho^{HF}} - \overline{z_r(\rho, t) \bar{\mathbf{v}} \cdot \nabla \rho^{HF}} dV, \quad (31)$$

Note that we have used the following relation to obtain the conversion terms formulas:

$$\begin{aligned} \int_V \overline{z_r(\rho, t) \bar{\mathbf{v}} \cdot \nabla (\bar{\rho} + \rho^{LF} + \rho^{HF})} dV = \\ \int_V \overline{z_r(\rho, t) \mathbf{v}^{HF} \cdot \nabla (\bar{\rho} + \rho^{LF} + \rho^{HF})} dV = \int_V \overline{z_r(\rho, t) \mathbf{v}^{LF} \cdot \nabla (\bar{\rho} + \rho^{LF} + \rho^{HF})} dV = 0. \end{aligned} \quad (32)$$

The dissipation of BPE (Hughes et al. 2009; Zemskova et al. 2015) for each frequency band * is:

$$D_{BPE^*} = \int_V \overline{g z_r(\rho, t) D^*} dV, \quad (33)$$

and the forcing of the mean BPE is:

$$F_{BPE^{MEAN}} = \int_V \overline{g z_r(\rho, t) \bar{F}} dV \quad (34)$$

256 The advantage of this approach compared to that of Zemskova et al. (2015) is that the time inde-
 257 pendent heat flux forcing is entirely contained in BPE^{MEAN} and that we have explicit equations
 258 for the densities associated with BPE^{LF} and BPE^{HF} .

259 In the three MITgcm configurations described in the following section 3, the diffusive pro-
 260 cesses increase the mean BPE ($D_{BPE^*} > 0$) and the surface heat flux forcing acts to decrease it
 261 ($F_{BPE^{MEAN}} < 0$). Because the APE varies in opposition to the BPE the above mentioned forcing
 262 and dissipation have respectively an increasing and decreasing impact on the APE. The sign of the
 263 forcing and dissipation of BPE is consistent with results from previous studies using BPE (Hughes
 264 et al. 2009; Zemskova et al. 2015).

265 *c. Available potential energy*

266 The mean APE budget is obtained as the difference between the mean PE (Eq. (9)) and the mean
 267 BPE (Eq. (26)) budgets:

$$\begin{aligned}
 \frac{dAPE^{MEAN}}{dt} &= \frac{dPE^{MEAN}}{dt} - \frac{dBPE^{MEAN}}{dt} = \\
 &= \underbrace{-C(APE^{MEAN}, APE^{LF})}_{=-C(PE^{MEAN}, PE^{LF}) + C(BPE^{MEAN}, BPE^{LF})} \underbrace{-C(APE^{MEAN}, APE^{HF})}_{=-C(PE^{MEAN}, PE^{HF}) + C(BPE^{MEAN}, BPE^{HF})} \\
 &\quad \underbrace{-C(APE^{MEAN}, KE^{MEAN})}_{=-C(PE^{MEAN}, KE^{MEAN})} + \underbrace{D_{APE^{MEAN}}}_{=D_{PE^{MEAN}} - D_{BPE^{MEAN}}} + \underbrace{F_{APE^{MEAN}}}_{=-F_{BPE^{MEAN}}} \quad (35)
 \end{aligned}$$

268 The conversion, dissipation and forcing terms of PE and BPE are derived in the two previous
 269 sections. Because $APE^{MEAN} = PE^{MEAN} - BPE^{MEAN}$, the evolution terms of BPE^{MEAN} appear
 270 in the APE^{MEAN} budget with a minus sign. $D_{APE^{MEAN}}$ can then either be seen as the dissipation
 271 of mean APE or as the conversion between mean APE and mean BPE due to the time mean
 272 diffusive flux. Note that $D_{PE^{MEAN}}$ does not explicitly appear in the BPE budget but it can be argued
 273 (see Hughes et al. 2009) that it contributes to the BPE budget and is thus added here as part of

274 $D_{APE^{MEAN}}$. Similarly, $F_{APE^{MEAN}}$ can be seen as the forcing of mean APE or as the conversion of
 275 (mean) BPE to APE due to surface heat flux.

276 Because there is no potential energy in anomalies, APE in anomalies is only made of BPE. The
 277 LF APE budget is then:

$$\begin{aligned} \frac{dAPE^{LF}}{dt} &= \frac{dPE^{LF}}{dt} - \frac{dBPE^{LF}}{dt} = \\ &= \underbrace{-C(APE^{LF}, KE^{LF})}_{=-C(PE^{LF}, KE^{LF})} + \underbrace{C(APE^{MEAN}, APE^{LF})}_{=C(PE^{MEAN}, PE^{LF}) - C(BPE^{MEAN}, BPE^{LF})} - \underbrace{C(APE^{LF}, APE^{HF})}_{=C(BPE^{LF}, BPE^{HF})} + \underbrace{D_{APE^{LF}}}_{=-D_{BPE^{LF}}}. \end{aligned} \quad (36)$$

278 Similarly, the HF APE budget is:

$$\begin{aligned} \frac{dAPE^{HF}}{dt} &= \frac{dPE^{HF}}{dt} - \frac{dBPE^{HF}}{dt} = \\ &= \underbrace{-C(APE^{HF}, KE^{HF})}_{=-C(PE^{HF}, KE^{HF})} + \underbrace{C(APE^{MEAN}, APE^{HF})}_{=C(PE^{MEAN}, PE^{HF}) - C(BPE^{MEAN}, BPE^{HF})} + \underbrace{C(APE^{LF}, APE^{HF})}_{=-C(BPE^{LF}, BPE^{HF})} + \underbrace{D_{APE^{HF}}}_{=-D_{BPE^{HF}}}. \end{aligned} \quad (37)$$

279 *d. Kinetic Energy*

280 In this subsection, the budgets for the total and low frequency kinetic energy are derived. The
 281 horizontal momentum equations are:

$$\frac{\partial u}{\partial t} + \mathbf{v} \cdot \nabla u - fv = -\frac{1}{\rho_0} \frac{\partial p}{\partial x} + V_u + F_u \quad (38)$$

$$\frac{\partial v}{\partial t} + \mathbf{v} \cdot \nabla v + fu = -\frac{1}{\rho_0} \frac{\partial p}{\partial y} + V_v \quad (39)$$

282 where p is the pressure, V_u and V_v are the viscous term in respectively the zonal and meridional
 283 direction, F_u is the zonal, time-independent forcing (we assume no meridional forcing) and f is the
 284 Coriolis parameter. Time averaging Eqs. (38) and (39), multiplying by $\rho_0 \bar{u}$ and $\rho_0 \bar{v}$ and summing

285 give an equation for the local kinetic energy of the time mean flow:

$$\begin{aligned} \frac{\rho_0}{2} \bar{\mathbf{v}} \cdot \nabla (\bar{u}^2 + \bar{v}^2) = & -\rho_0 \bar{u} \nabla \cdot (\overline{\mathbf{v}^{\text{HF}} u^{\text{HF}} + \mathbf{v}^{\text{LF}} u^{\text{LF}}}) - \rho_0 \bar{v} \nabla \cdot (\overline{\mathbf{v}^{\text{HF}} v^{\text{HF}} + \mathbf{v}^{\text{LF}} v^{\text{LF}}}) \\ & - \nabla \bar{p} - g \bar{\rho} \bar{w} + \rho_0 \bar{u} \bar{V}_u + \rho_0 \bar{v} \bar{V}_v + \rho_0 \bar{u} \bar{F}_u \end{aligned} \quad (40)$$

286 The Coriolis term does not play any part in the kinetic energy budget because the Coriolis accel-
 287 eration is normal to the velocity and there is no contribution from the vertical velocity because
 288 the hydrostatic approximation is used and implies no vertical acceleration (Gregory and Tailleux
 289 2011). Integrating (40) over the entire volume gives the budget for KE^{MEAN} :

$$\begin{aligned} \frac{dKE^{\text{MEAN}}}{dt} = & C(APE^{\text{MEAN}}, KE^{\text{MEAN}}) \\ & - C(KE^{\text{MEAN}}, KE^{\text{LF}}) - C(KE^{\text{MEAN}}, KE^{\text{HF}}) + D_{KE^{\text{MEAN}}} + F_{KE^{\text{MEAN}}} \end{aligned} \quad (41)$$

290 where:

$$C(APE^{\text{MEAN}}, KE^{\text{MEAN}}) = - \int_V g \bar{\rho} \bar{w} dV \quad (42)$$

$$C(KE^{\text{MEAN}}, KE^{\text{LF}}) = \int_V \overline{\rho_0 \bar{u} \nabla \cdot (\mathbf{v}^{\text{LF}} u^{\text{LF}}) + \rho_0 \bar{v} \nabla \cdot (\mathbf{v}^{\text{LF}} v^{\text{LF}})} dV \quad (43)$$

$$C(KE^{\text{MEAN}}, KE^{\text{HF}}) = \int_V \overline{\rho_0 \bar{u} \nabla \cdot (\mathbf{v}^{\text{HF}} u^{\text{HF}}) + \rho_0 \bar{v} \nabla \cdot (\mathbf{v}^{\text{HF}} v^{\text{HF}})} dV \quad (44)$$

$$D_{KE^{\text{MEAN}}} = \int_V \rho_0 \bar{u} \bar{V}_u + \rho_0 \bar{v} \bar{V}_v dV \quad (45)$$

$$F_{KE^{\text{MEAN}}} = \int_V \rho_0 \bar{u} \bar{F}_u dV \quad (46)$$

295 Proceeding similarly for the LF and HF, we obtain the following budgets for KE^{LF} and KE^{HF} :

$$\frac{dKE^{\text{LF}}}{dt} = C(APE^{\text{LF}}, KE^{\text{LF}}) + C(KE^{\text{MEAN}}, KE^{\text{LF}}) - C(KE^{\text{LF}}, KE^{\text{HF}}) + D_{KE^{\text{LF}}} \quad (47)$$

$$\frac{dKE^{\text{HF}}}{dt} = C(APE^{\text{HF}}, KE^{\text{HF}}) + C(KE^{\text{MEAN}}, KE^{\text{HF}}) + C(KE^{\text{LF}}, KE^{\text{HF}}) + D_{KE^{\text{HF}}} \quad (48)$$

$$C(APE^{\text{LF}}, KE^{\text{LF}}) = - \int_V g \bar{\rho}^{\text{LF}} \bar{w}^{\text{LF}} dV \quad (49)$$

$$C(APE^{HF}, KE^{HF}) = - \int_V g \overline{\rho^{HF} w^{HF}} dV \quad (50)$$

$$C(KE^{LF}, KE^{HF}) = - \int_V \overline{\rho_0 u^{HF} \nabla (\mathbf{u}^{HF} u^{LF}) + \rho_0 u^{HF} \nabla (\mathbf{u}^{HF} u^{LF})} dV \quad (51)$$

$$D_{KE^{LF}} = \int_V \overline{\rho_0 u^{LF} V_u^{LF} + \rho_0 v^{LF} V_v^{LF}} dV \quad (52)$$

$$D_{KE^{HF}} = \int_V \overline{\rho_0 u^{HF} V_u^{HF} + \rho_0 v^{HF} V_v^{HF}} dV \quad (53)$$

e. Practical calculation of the APE/KE budget using model outputs

In Table 1 we describe how each term of the KE and APE budget mapped in figure 3 is computed using results from the previous subsections. Due to the very long timescales of the LF variability (~ 50 years) it would require too much storage to resolve the HF terms. However we show below that the HF budgets can be obtained as the residual of the well-resolved LF budgets. As explained above, APE forcing and dissipation can also be seen as conversion between BPE and APE reservoirs. This is shown in figure 3 by the addition of a BPE reservoir that exchanges energy with the three APE reservoirs.

The total conversion from APE to KE can be obtained from the time mean advection of the temperature which is an output of the model:

$$C(APE, KE) = \int_V g z \nabla \overline{\rho} dV = \underbrace{\int_V g \nabla (z \overline{\rho}) dV}_{=0} - \int_V g \overline{w \rho} dV \quad (54)$$

$C(APE^{HF}, KE^{HF})$ can then be deduced from the knowledge of $C(APE^{LF}, KE^{HF})$ and $C(APE^{MEAN}, KE^{MEAN})$:

$$C(APE^{HF}, KE^{HF}) = C(APE, KE) - C(APE^{LF}, KE^{HF}) - C(APE^{MEAN}, KE^{MEAN}). \quad (55)$$

$D_{KE^{HF}}$ is obtained from the total KE budget:

$$D_{KE^{HF}} = -C(APE, KE) - F_{KE^{MEAN}} - D_{KE^{MEAN}} - D_{KE^{LF}}. \quad (56)$$

313 $D_{APE^{HF}}$ is obtained using the total APE budget:

$$D_{APE^{HF}} = C(APE, KE) - F_{APE^{MEAN}} - D_{APE^{MEAN}} - D_{APE^{LF}}. \quad (57)$$

314 Similarly, $C(KE^{LF}, KE^{HF})$ is obtained from the KE^{LF} budget, $C(KE^{MEAN}, KE^{HF})$ from the
 315 KE^{MEAN} budget, $C(APE^{LF}, APE^{HF})$ from the APE^{LF} budget, and $C(APE^{MEAN}, APE^{HF})$ from
 316 the APE^{MEAN} budget.

317 **3. Model and configuration**

318 We use the MITgcm (Marshall et al. 1997) in a rectangular flat-bottom basin with a Carte-
 319 sian geometry on a β -plane centered at 40°N . The zonal and meridional extents are respectively
 320 $L_x = 5000\text{km}$ and $L_y = 4500\text{km}$, and the Southern boundary is located 2000km north of the equa-
 321 tor. An eddy-permitting horizontal resolution of 20km is used in both directions. This resolution
 322 is sufficient in Huck et al. (2015) to capture the main characteristics of the effect of eddy turbu-
 323 lence on low-frequency variability. The depth is $H = 4500\text{m}$, there are 40 levels on the vertical
 324 with grid spacing increasing from 10m at the surface to 400m at the bottom.

325 The ocean is forced by constant heat flux at the surface, decreasing linearly with latitude from
 326 50W m^{-2} at $y = 0\text{km}$ to -50W m^{-2} at $y = 4500\text{km}$, similar to Huck et al. (2015). Static instabil-
 327 ity is removed by strong vertical mixing of the water column. We use biharmonic horizontal eddy
 328 diffusivity with a uniform value of $10^{11}\text{m}^4\text{s}^{-1}$ and Leith implicit viscosity. The vertical viscosity
 329 is $\nu_v = 10^{-3}\text{m}^2\text{s}^{-1}$. In this single hemisphere configuration, the strength of the Meridional Over-
 330 turning Circulation (MOC) is a strong function of the vertical diffusivity K_v , in agreement with the
 331 $K_v^{1/2}$ geostrophic scaling (Huang and Chou 1994). Here, we choose to use $K_v = 2 \times 10^{-4}\text{m}^2\text{s}^{-1}$
 332 corresponding to a MOC strength close to 10 Sv . Because the primary objective of this study is
 333 to establish and understand the full energy budget of the low-frequency mode in the configuration

used in previous published articles (Huck et al. 1999, 2001, 2015; Hochet et al. 2020) our main experiment does not have wind forcing. However we also perform two additional experiments with increasing wind forcing intensity to study the effect of a direct KE source on the energy budget. The zonal wind stress used in the two wind forcing experiments varies with latitude according to the following formula:

$$\tau_x(y) = \tau_0 \left(\frac{1}{4} \cos \left(\frac{y\pi}{L_y} \right) - \cos \left(\frac{2\pi y}{L_y} \right) \right), \quad (58)$$

where τ_0 is the wind stress amplitude. The meridional wind stress is zero. We chose to use a non-symmetric zonal wind stress as it seems important to achieve a generic dynamical behavior of the double-gyre circulation (Berloff and McWilliams 1999). The three experiments use $\tau_0 = 0 \text{ N m}^{-2}$ (no wind forcing), $\tau_0 = 0.05 \text{ N m}^{-2}$ (intermediate wind) and $\tau_0 = 0.1 \text{ N m}^{-2}$ (climatological wind) (Fig. 4). All three experiments are initialized with a state of rest, the spin-up time is then 500 years and the model is run for another 400 years to produce outputs to compute the diagnostics presented below.

4. Time mean circulation and variability

In the following section we describe the time mean circulation as well as the low and high frequency variability obtained for the range of surface wind-stress forcing amplitudes mentioned above. Hochet et al. (2020) used exactly the same model parameters and configuration as the present study with zero wind-stress forcing. The turbulent transfer of temperature variance in their study was shown to act as a source of temperature variance for frequencies higher than 1/3.5 years and a sink for smaller frequencies. We thus define the limit between low and high frequencies as being 3.5 yr. Although it is possible that this limit is altered by the surface wind stress that we use in the two other experiments, we keep the same definition of 1/3.5 years in all experiments to be able to compare the three configurations. We thus associate LF with multi-decadal, decadal

and part of the inter-annual variability and HF with part of the inter-annual and eddy turbulence induced variability.

a. No wind forcing $\tau_0 = 0 \text{ N m}^{-2}$

Note that the simulation used in this subsection (i.e. without wind forcing) is the same as that described in Hochet et al. (2020), and the description of the LF variability is reproduced below. In the absence of wind-stress forcing, LF variability spontaneously develops with a significant and narrow peak frequency of $1/53 \text{ yr}^{-1}$ (Fig. 5). A detailed description of the variability developing in very similar geometries can be found for instance in Huck et al. (1999) and Huck et al. (2015). Here we will only give a short description of its main characteristics. Following Hochet et al. (2020), we use Complex Empirical Orthogonal Function (CEOF) to describe the LF variability of the three dimensional temperature field. The CEOF are calculated using 50-day average outputs on a 400-year long simulation. The 400 year is chosen to obtain a statistical equilibrium of the solution. Similar to the widely used empirical orthogonal function, CEOF are the eigenvectors of the complex covariance matrix of a complex temperature anomaly which is calculated using the Hilbert transform of the detrended temperature anomaly (Von Storch and Zwiers 2001). The leading CEOF contains 60% of the temperature variance (Fig. 6). The temperature anomaly associated to a CEOF can then be reconstructed using the following formula:

$$\theta_{\text{CEOF}}(x, y, z, t) = \text{PC}_{re}(t)\text{CEOF}_{re}(x, y, z) + \text{PC}_{im}(t)\text{CEOF}_{im}(x, y, z) \quad (59)$$

where *re* and *im* stand for the real and imaginary parts respectively and PC is the principal component of the corresponding CEOF. The APE is shown along with the real and imaginary part of the PC (Fig. 6). The phase of the leading CEOF is chosen to match that of the APE time variation. The APE is very well correlated with the real part of the PC and shows that APE multidecadal vari-

377 ations are linked with the SST pattern shown on the upper panel of figure 6. The low-frequency
 378 variability takes the form of a large-scale temperature anomaly, located mainly in the northwestern
 379 half and in the upper 500 m of the basin with SST anomaly larger than 3 K at some locations (Fig.
 380 6). The successive positions of the positive and negative temperature anomalies as shown on figure
 381 6, i.e. a negative center located at latitudes around 2500-3000km and longitude 2000km (opposite
 382 of the imaginary part), followed by a negative center for latitudes between 3000 and 3500 km,
 383 longitude around 2000 km (real part), then a negative center around latitude 4000 km, longitude
 384 1500km (imaginary part), then a negative center in the north western corner (opposite of the real
 385 part), indicate north-westward propagation of the temperature anomalies.

386 The sea surface height (SSH) varies together with the temperature anomalies of the leading
 387 CEOF (left column of Fig. 7). The amplitude of SSH anomalies (15-20 cm) is maximum along
 388 the western boundary current and in its eastward extension in the northern-half of the basin. These
 389 values compare well with altimetric observations (Stammer 1997). The time mean of the vertical
 390 integral of the LF APE and of the LF density variance are shown in figure 7. The largest values for
 391 the LF APE are located along the northern boundary. Equation (22) shows that large values of LF
 392 APE (=LF BPE) are associated with deep reference depth and thus outcropping of dense waters.
 393 The location of LF APE contrasts with the location of the largest values of LF density variance
 394 which are located in the northern part of the basin interior (Fig. 7). The differences between these
 395 two quantities further demonstrate that the APE cannot be approximated by the density variance
 396 in these configurations in contrast with QG theory.

397 *b. Intermediate wind forcing $\tau_0 = 0.05 \text{ N m}^{-2}$*

398 When wind-stress forcing is present the temperature variability is significantly reduced com-
 399 pared to the previous case and consists of a broad band of low-frequency signals with a peak

frequency of about $1/22 \text{ yr}^{-1}$ (Fig. 5). Huck et al. (2001) explained this effect of the wind forcing on the low frequency variability by the damping effect of the Ekman pumping on the large-scale anomalies. To explain this effect, Huck et al. (2001) assumed that the following formula describes the effect of wind stress on the temperature anomalies (their equation (14)):

$$\frac{\partial \theta'}{\partial t} = -W_E \frac{\partial \theta'}{\partial z} \quad (60)$$

where θ' is the temperature anomaly, and W_E the Ekman pumping. Then if θ' is further assumed to have an exponential profile with depth, $\theta' \propto \exp(-W_E k t)$ with k of the order of 500 m^{-1} . The temperature anomaly decreases where W_E is positive which is in the Northern half of the basin in our configuration.

The surface signature of the leading CEOF of temperature variability, explaining 28% of the spatially integrated variance, shows that the variability now occurs predominantly along the eastern boundary and along a narrow latitudinal band extending across the width of the basin just south of the intergyre boundary (Fig. 8). The large-scale anomaly emanates from the eastern boundary and propagates to the west along the mean temperature contours. SSH variability is no longer collocated with SST variations, as was the case with zero wind-stress forcing, but instead mostly occurs along a region centered about the intergyre (at $y = 2000 \text{ km}$) along the western boundary (Fig. 7, second row). The LF density variance is now almost entirely located on the eastern boundary as also shown by the CEOF (Fig. 8). The LF APE is in the northeastern corner of the basin in the region where dense waters outcrop.

418 *c. Climatological wind forcing $\tau_0 = 0.1 \text{ N m}^{-2}$*

Increasing the amplitude of the zonal surface wind-stress forcing up to realistic values has the effect of further decreasing (increasing) the temperature variance on interdecadal (monthly

421 to interannual) timescales compared to the case with $\tau_0 = 0.05 \text{ N m}^{-2}$. Indeed the volume av-
 422 eraged LF (HF) temperature spectrum (defined as frequencies lower than $\frac{2\pi}{3.5\text{years}}$) is weaker for
 423 $\tau_0 = 0.05 \text{ N m}^{-2}$ than for $\tau_0 = 0.1 \text{ N m}^{-2}$ (Fig. 5).

424 The leading CEOF of temperature variability now represents only 7% of the spatially-integrated
 425 variance and is mostly apparent south of the intergyre boundary (Fig. 9). This pattern of variability
 426 differs from the previous case with $\tau_0 = 0.05 \text{ N m}^{-2}$ (Fig. 8) for which SST variability was also
 427 present along the eastern boundary. SSH variability however shares the same pattern and amplitude
 428 as that obtained for $\tau_0 = 0.05 \text{ N m}^{-2}$ with enhanced variability along the western boundary current.
 429 The LF APE is now located in the northwestern part of the basin with a much smaller amplitude
 430 than in the two previous cases.

431 5. Energy budget

432 We now describe the mean, LF, and HF KE, APE and BPE budgets for the three experiments
 433 described above, summarized in figures 10,12, and 13 following the schematic given in figure 3.
 434 Table 2 gathers the transfer values obtained for the three experiments.

435 a. No-wind forcing $\tau_0 = 0 \text{ N m}^{-2}$

436 In the absence of surface wind-stress there is no external source for the KE reservoir and the main
 437 energy pathways are located within the APE part of the budget (Fig. 10). Among the 119 GW of
 438 conversion between BPE and APE due to surface heat flux 32 GW is converted into KE (mainly
 439 at HF) where it is dissipated by viscous forces. The remaining 87 GW are mainly transferred from
 440 HF APE to BPE because of dissipation (53 GW from APE HF to BPE, 16GW from LF APE to
 441 BPE and 18 GW from mean APE to BPE).

442 Despite the differences between BPE and density variance shown in figure 7, Hochet et al. (2020)
 443 found a similar pathway for the temperature variance. The surface heat flux is the only source of
 444 mean temperature variance and LF temperature variance is forced through a transfer of temperature
 445 variance from the mean flow, this transfer is interpreted as the result of baroclinic instability of the
 446 mean flow. The conversion from mean APE to LF APE is 49GW which is the largest conversion
 447 term in this experiment. The main sink of LF APE is the conversion to HF APE (29 GW), whereas
 448 the dissipation removes 16GW. Because the direction of the LF/HF APE transfer is from LF to HF
 449 and because LF are associated with large scales and HF with mesoscale eddies, we deduce that
 450 mesoscale eddy turbulence is a sink of energy for the low-frequency variability which is one of the
 451 main result of this study. It confirms previous findings of Arbic et al. (2014) who demonstrated the
 452 existence of a direct temporal APE cascade along with the inverse temporal KE cascade under QG
 453 approximation. Conversion between kinetic energy reservoirs is small compared to conversion
 454 between APE reservoirs. There is however a substantial energy transfer (20 GW) between HF
 455 APE and HF KE. This input of HF KE is balanced by the sink linked with viscous terms. The
 456 only source of mean KE is the conversion of mean APE to mean KE (8GW) and the conversion
 457 between LF and HF KE is negligible. The ratio of LF KE to LF APE is of 0.3% showing that the
 458 low frequency variability is predominantly found in APE in this simulation.

459 The two left columns of Fig. 11 show the spatial pattern of $C(APE^{MEAN}, APE^{HF})$,
 460 $C(APE^{MEAN}, APE^{LF})$ integrated vertically over the water column. Strong positive values of
 461 these two terms are generally located close to the northern boundary, where the convection is the
 462 strongest. Positive values of $C(APE^{MEAN}, APE^{HF})$ are located in the eastern part of the northern
 463 boundary and follows closely the values of mean APE forcing (last column of Fig. 11). Negative
 464 values are located in the southern part of the basin interior. The mean APE forcing term is large
 465 in regions where the reference level is the deepest i.e. where dense waters outcrop at the surface.

$C(APE^{MEAN}, APE^{LF})$ (Fig. 11, middle-left column) has its largest values close to the northern and eastern boundary. The vertical integral of the term $-\overline{\mathbf{u}^{LF} \rho^{LF}} \cdot \nabla \bar{\rho}$ which represents the transfer from the mean to the LF density variance (see Colin de Verdière and Huck 1999, for instance) is shown on the third column of figure 11 and is very different from $C(APE^{MEAN}, APE^{LF})$. This could be expected from the difference between the variance of the LF density and the LF APE already shown in figure 7: the transfer from mean APE to LF APE occurs in the convection region where dense waters outcrop whereas the LF density variance transfer occurs in the basin interior. $C(APE^{LF}, APE^{HF})$ is not shown but follows closely the variation of $C(APE^{MEAN}, APE^{LF})$.

b. Intermediate wind forcing $\tau_0 = 0.05 \text{ N m}^{-2}$

With an intermediate zonal wind stress at the surface, the LF variability becomes weaker and shifts to mid-latitudes as explained in section 4 b. The energy budget (Fig. 12) shows a decrease of the energy fluxes from mean APE and LF APE. The transfer of BPE to mean APE is the same as that obtained for the no-wind experiment (119GW). Part of this mean APE energy input is transferred back to BPE by parametrized diffusive flux (30GW) whereas most of it is converted into HF APE (61GW). The conversion of LF APE to HF APE is approximately half the value obtained for the no-wind case (14GW against 29GW). The total transfer (i.e. KE+APE) is still directed from LF toward HF. There is now a small direct forcing of mean KE (7GW) which adds to the conversion from mean APE to mean KE (5GW) to create a source of 12GW of Mean KE. 8GW is directly dissipated by viscous forces, the remaining is mainly transferred to HF KE. The conversion between LF KE and HF KE is negligible.

The ratio of LF KE and LF APE has increased compared with the no wind simulation (the ratio is now 1%), however LF KE remains negligible compared to LF APE. We explain the predominance of APE over KE in the LF by the larger scales found at these frequencies. It is indeed known

from QG theory that the ratio KE over APE decreases with larger scales (Vallis 2017). Using the ECCO2 ocean state estimate, Zemskova et al. (2015) found that there is approximately 10 times more APE than KE in anomalies but do not discriminate between frequency bands which make the comparison with our results difficult.

With wind forcing, the $C(APE^{MEAN}, APE^{HF})$ conversion increases by 17GW (Table 2), its positive values follow the northern boundary of the basin (Fig. 11) and the mean APE forcing (last column of Fig. 11). The largest values of $C(APE^{MEAN}, APE^{LF})$ are now almost entirely located in the northeastern corner where the SST anomalies seem to originate from.

497 *c. Climatological wind forcing $\tau_0 = 0.1 \text{ N m}^{-2}$*

In this experiment the zonal wind forcing is twice as strong as in the previous experiment, close to the climatological amplitude. The wind stress adds 34GW to the mean KE reservoir and 15 GW is directly dissipated by viscous forces (Fig. 13). The conversion from mean APE to mean KE is now negative (i.e. from mean KE to mean APE) which is in line with what is calculated in OGCM (e.g. Toggweiler and Samuels 1998; Gnanadesikan et al. 2005; Gregory and Tailleux 2011). The remaining 8GW are all converted to HF KE. The conversion of BPE to mean APE due to heat flux has slightly increased compared to the two other experiments (128GW). The BPE to mean APE conversion formula $-g \int_V \overline{z_r(\rho, t)} \overline{F} dV$ shows that the value of this conversion mainly depends on the position of the deepest reference depths and thus on the circulation in the Northern half of the basin. An explanation for the (small) increase in BPE to mean APE conversion could thus be that only the climatological wind substantially modifies the circulation in this region. The conversion from mean APE to HF APE is now much larger than the conversion from mean APE to LF APE (84GW vs 13GW), 42 GW is directly dissipated. The energy in the LF KE reservoir has increased compared to the two other simulation and now represents 10% of LF APE.

512 With this realistic amplitude of wind forcing, positive values of the conversion
 513 $C(APE^{MEAN}, APE^{HF})$ continue to extend along the northern boundary (Fig. 11 bottom line) and
 514 is particularly intense in the northwestern corner. $C(APE^{MEAN}, APE^{LF})$ intensity is weaker than
 515 before and almost entirely located in the northwestern corner.

516 Sohail et al. (2018) and Zemskova et al. (2021) report that the input of KE obtained by increas-
 517 ing the wind stress over the Southern ocean results mainly in an increase of the KE dissipation
 518 term, rather than an increase in APE dissipation. These results are in line with what is found in
 519 our experiments: the total dissipation of KE ($D_{KE^{MEAN}} + D_{KE^{LF}} + D_{KE^{HF}}$) has increased by 65%
 520 between the no-wind and climatological wind experiment and by 24% for the total dissipation of
 521 APE ($D_{APE^{MEAN}} + D_{APE^{LF}} + D_{APE^{HF}}$): most of the additional mean KE forcing is directly dissi-
 522 pated by KE total dissipation.

523 6. Conclusion

524 In this article we have derived the mechanical energy budget for the large-scale, internally gener-
 525 ated, low-frequency ocean mode that was studied extensively in previous works (Colin de Verdière
 526 and Huck 1999; Huck et al. 1999; Huck and Vallis 2001; Huck et al. 2001, 2015; Arzel et al. 2018;
 527 Hochet et al. 2020). The mechanical energy budget is decomposed into mean, low-frequency, and
 528 high-frequency parts to study the effect of the large-scale baroclinic instability of the mean circu-
 529 lation and the effect of the eddy field on the LF mode. One of the main achievements of this work
 530 is the new way of decomposing the background potential energy into frequency bands that allows
 531 us to correctly attribute the source and sink terms associated with each reservoir.

532 The energy budget of the no wind experiment shows that the energy of this multidecadal mode
 533 is mostly contained in the LF APE rather than in the LF KE because of its large-scale. Using
 534 ECCO v2, Zemskova et al. (2015) also found that the energy is mostly contained in the fluctuating

535 APE rather than in the fluctuating KE, but with a smaller ratio of approximately 10 (compared to
 536 a LF APE over LF KE ratio of approximately 300 in our no wind experiment). This difference is
 537 probably due to our use of a single hemispheric basin and thus to the omission of the strong wind
 538 forcing over the Southern ocean. The source term for the LF APE is the conversion from the mean
 539 APE to the LF APE. In agreement with Hochet et al. (2020) where the budget was made in terms
 540 of temperature variance, the sink term of the mode is attributed to the parametrized diffusion (\sim
 541 36 %) and to the transfer of APE to higher-frequencies linked with mesoscale eddy turbulence (\sim
 542 64 %). In the experiment with no wind forcing, the only source of kinetic energy is the conversion
 543 from APE at all frequencies. The transfer of KE between high and low-frequencies which is
 544 shown to be an important source of low frequency variability in other experiments (Arbic et al.
 545 2014; Sérazin et al. 2018) appears negligible in our configuration compared to all the other energy
 546 fluxes. Recognising that this might be due to the absence of any direct source of kinetic energy we
 547 performed two other experiments with a time independent zonal wind forcing at the surface that
 548 drives the classical wind-driven double gyres.

549 With the addition of a wind forcing at the surface, a source term for the mean kinetic energy
 550 appears. The structure of the LF mode is modified with intermediate wind strength and almost
 551 disappears with climatological wind. With increasing wind forcing, the LF APE and all its asso-
 552 ciated conversion terms decrease. Indeed there is a decrease in the values of the conversion terms
 553 from mean APE to LF APE and of LF APE to BPE (linked with diffusive flux), of LF APE to
 554 HF APE and of LF APE to LF KE for the sink terms. Meanwhile, the energy in the HF APE
 555 increases as well as the conversion from mean APE to HF APE. This larger conversion is balanced
 556 mostly by a larger conversion of HF APE to BPE due to diffusive flux. The energy contained in
 557 the mean APE increases as well as the conversion from BPE to mean APE due to heat flux. This
 558 increase is balanced by a larger conversion to BPE due to diffusive flux and by a larger conversion

559 to HF APE. The conversion of mean APE to mean KE becomes negative which is in agreement
560 with what is usually calculated in more realistic models such as in Zemskova et al. (2015). The
561 conversion between LF KE and HF KE remains negligible or very small compared to other con-
562 versions, nonetheless, it is directed from HF to LF for the climatological wind experiment which
563 is in agreement with the temporal inverse KE cascade found in Arbic et al. (2014).

564 For all wind stress intensities studied here, the energy and conversion terms remain mainly con-
565 tained in the APE. There is however a non-negligible transfer of APE to KE at HF where it is
566 dissipated by viscous forces. The fact that most of the transfers of energy occur between the dif-
567 ferent APE and BPE reservoirs rather than between PE or KE reservoirs outline the importance of
568 the APE budget to study large-scale and low frequency variability. In contrast, Arbic et al. (2014);
569 Sérazin et al. (2015, 2018) found a predominant role for the temporal inverse KE cascade, but we
570 attribute this difference for the most part to our focus on multidecadal variability as compared to
571 their focus on shorter inter-annual variability. The transfer from LF APE to HF APE demonstrates
572 the damping role of the mesoscale eddy turbulence for the large scale variability, even for realistic
573 wind intensities. This transfer of APE from LF to HF is very similar to the QG APE direct tempo-
574 ral cascade of APE that has been observed (along with the inverse temporal cascade of KE) in the
575 idealized simulation of Arbic et al. (2014). Temperature variance budget gives similar pathway
576 for the sources and sinks of the low frequency mode (Hochet et al. 2020). However, we have shown
577 that the locations of the APE and of its associated transfers differ significantly from that of the den-
578 sity variance. Large values of APE are indeed linked with the outcropping of dense waters at the
579 surface due to convection that occurs along the northern boundary in our configuration, whereas
580 there is no significant link between large values of density variance and convective regions. The
581 APE budget is therefore more accurate in identifying regions where energy conversions are the
582 most important.

583 This study is limited by several approximations, the first being the representation of the North
 584 Atlantic ocean with a simplified geometry and a flat bottom. In particular, the wind forcing over
 585 the Southern Ocean is thought to play an important role in setting the mean stratification, in par-
 586 ticular the stratification in the North Atlantic (e.g. Nikurashin and Vallis 2011, 2012) and might
 587 therefore influence the dynamic of the low frequency mode. Moreover, using energy budget of
 588 a global ocean–sea ice model Hogg et al. (2017) have shown that wind change over the South-
 589 ern Ocean leads to change of APE and stratification in the North Atlantic. However, it has been
 590 shown in Arzel et al. (2007) that the addition of a re-entrant channel representing the Antarctic
 591 Circumpolar Current acts to reduce the low frequency variability in the Southern Hemisphere but
 592 does not suppress the internal variability in the Northern Hemisphere. Moreover, the physical
 593 mechanism giving rise to the internal mode studied in this single hemispheric configuration is also
 594 found to give rise to low-frequency variability in realistic ocean-only configuration (e.g. Sévellec
 595 and Fedorov 2013; Arzel et al. 2018; Arzel and Huck 2020) and in ocean-atmosphere coupled
 596 configuration (e.g. Ortega et al. 2015; Gastineau et al. 2018). The omission of salinity and the use
 597 of a linear equation of state for density certainly has an influence on the APE budget. Indeed, it
 598 is known that non-linearities of the equation of state are in general not negligible (e.g. Klocker
 599 and McDougall 2010; Nycander et al. 2015). Nonetheless, it has been shown in a realistic setup
 600 (Sévellec and Fedorov 2013) that the mode is largely controlled by temperature variation in the
 601 upper ocean. Our study as well as previous studies of the internal mode (e.g. Sévellec and Fe-
 602 dorov 2013; Huck et al. 2015; Arzel et al. 2018) assume that external forcing is either constant or
 603 made of natural variability such as the North Atlantic Oscillation (Frankcombe et al. 2009; Arzel
 604 and Huck 2020). This assumption is helpful to understand the physics and the mechanisms of the
 605 mode. However, with its multi-decadal variability, the internal mode might be affected by anthro-

606 pogenic forcing which act on the same time scales and modifies the characteristics of the ocean
607 stratification (Levitus et al. 2012).

608 The eddy-permitting resolution of 20 km used here is not sufficient to entirely resolve the eddy
609 field, however similar experiments at 10 km with no wind forcing were conducted in Huck et al.
610 (2015) and no qualitative differences were found. Lastly we set the limit between LF and HF to be
611 3.5 years based on the results from Hochet et al. (2020) that showed that in the same configuration
612 without wind forcing, non-linear transfers of temperature variance are a source (sink) term for
613 periods longer (shorter) than 3.5 years. To be able to compare the three configurations studied in
614 this article we kept this limit fixed, however, with the addition of a wind forcing at the surface, we
615 expect a change in this limit and possibly a modification of the LF/HF transfers. The study of the
616 dependence of this limit on external parameters is left to future work, as well as the implementation
617 of this full energy budget in realistic eddy-resolving models.

618 *Acknowledgments.* This study was supported by a EU Marie Curie IF grant number 749924.
619 Numerical computations were conducted using the Pôle de Calcul Intensif pour la Mer at Ifremer,
620 Brest, France. We thank the MITgcm development group for making their model freely available.
621 We also thank three anonymous reviewers for their comments and suggestions, which helped to
622 improve the manuscript.

623 **References**

624 Arbic, B. K., M. Müller, J. G. Richman, J. F. Shriver, A. J. Morten, R. B. Scott, G. Sérazin, and
625 T. Penduff, 2014: Geostrophic turbulence in the frequency–wavenumber domain: Eddy-driven
626 low-frequency variability. *Journal of Physical Oceanography*, **44** (8), 2050–2069.

Arzel, O., A. Colin de Verdière, and T. Huck, 2007: On the origin of interdecadal oscillations in a coupled ocean atmosphere model. *Tellus A*, **59** (3), 367–383.

Arzel, O., and T. Huck, 2020: Contributions of atmospheric stochastic forcing and intrinsic ocean modes to North Atlantic ocean interdecadal variability. *Journal of Climate*, **33** (6), 2351–2370.

Arzel, O., T. Huck, and A. Colin de Verdière, 2018: The internal generation of the Atlantic ocean interdecadal variability. *Journal of Climate*, **31** (16), 6411–6432, doi:10.1175/JCLI-D-17-0884.1.

Berloff, P. S., and J. C. McWilliams, 1999: Large-scale, low-frequency variability in wind-driven ocean gyres. *Journal of Physical Oceanography*, **29** (8), 1925–1949.

Booth, B. B., N. J. Dunstone, P. R. Halloran, T. Andrews, and N. Bellouin, 2012: Aerosols implicated as a prime driver of twentieth-century North Atlantic climate variability. *Nature*, **484** (7393), 228–232.

Buckley, M. W., D. Ferreira, J.-M. Campin, J. Marshall, and R. Tulloch, 2012: On the relationship between decadal buoyancy anomalies and variability of the Atlantic meridional overturning circulation. *Journal of Climate*, **25** (23), 8009–8030.

Clement, A., K. Bellomo, L. N. Murphy, M. A. Cane, T. Mauritsen, G. Rädel, and B. Stevens, 2015: The Atlantic Multidecadal Oscillation without a role for ocean circulation. *Science*, **350** (6258), 320–324.

Clement, A., M. A. Cane, L. N. Murphy, K. Bellomo, T. Mauritsen, and B. Stevens, 2016: Response to Comment on “The Atlantic Multidecadal Oscillation without a role for ocean circulation”. *Science*, **352** (6293), 1527–1527, doi:10.1126/science.aaf2575.

Colin de Verdière, A., and T. Huck, 1999: Baroclinic instability: An oceanic wavemaker for interdecadal variability. *Journal of Physical Oceanography*, **29** (5), 893–910.

Deser, C., M. A. Alexander, S.-P. Xie, and A. S. Phillips, 2010: Sea surface temperature variability: Patterns and mechanisms. *Annual review of marine science*, **2**, 115–143.

Frankcombe, L., H. Dijkstra, and A. Von der Heydt, 2008: Sub-surface signatures of the atlantic multidecadal oscillation. *Geophysical Research Letters*, **35** (19).

Frankcombe, L. M., H. A. Dijkstra, and A. Von der Heydt, 2009: Noise-induced multidecadal variability in the North Atlantic: Excitation of normal modes. *Journal of Physical Oceanography*, **39** (1), 220–233.

Frankignoul, C., and K. Hasselmann, 1977: Stochastic climate models, Part II Application to sea-surface temperature anomalies and thermocline variability. *Tellus*, **29** (4), 289–305.

Gastineau, G., J. Mignot, O. Arzel, and T. Huck, 2018: North Atlantic Ocean Internal Decadal Variability: Role of the Mean State and Ocean-Atmosphere Coupling. *Journal of Geophysical Research: Oceans*, **123** (8), 5949–5970.

Gnanadesikan, A., R. D. Slater, P. S. Swathi, and G. K. Vallis, 2005: The energetics of ocean heat transport. *Journal of climate*, **18** (14), 2604–2616.

Greatbatch, R. J., and S. Zhang, 1995: An interdecadal oscillation in an idealized ocean basin forced by constant heat flux. *Journal of climate*, **8** (1), 81–91.

Grégorio, S., T. Penduff, G. Sérazin, J.-M. Molines, B. Barnier, and J. Hirschi, 2015: Intrinsic variability of the atlantic meridional overturning circulation at interannual-to-multidecadal time scales. *Journal of Physical Oceanography*, **45** (7), 1929–1946.

Gregory, J. M., and R. Tailleux, 2011: Kinetic energy analysis of the response of the Atlantic meridional overturning circulation to CO₂-forced climate change. *Climate dynamics*, **37** (5-6), 893–914.

Gulev, S. K., M. Latif, N. Keenlyside, W. Park, and K. P. Koltermann, 2013: North atlantic ocean control on surface heat flux on multidecadal timescales. *Nature*, **499** (7459), 464–467.

Hasselmann, K., 1976: Stochastic climate models part I. Theory. *tellus*, **28** (6), 473–485.

Hochet, A., T. Huck, O. Arzel, F. Sévellec, A. Colin de Verdière, M. Mazloff, and B. Cornuelle, 2020: Direct temporal cascade of temperature variance in eddy-permitting simulations of multidecadal variability. *Journal of Climate*, **33** (21), 9409–9425.

Hogg, A. M., P. Spence, O. A. Saenko, and S. M. Downes, 2017: The energetics of southern ocean upwelling. *Journal of Physical Oceanography*, **47** (1), 135–153.

Huang, R. X., and R. L. Chou, 1994: Parameter sensitivity study of the saline circulation. *Climate Dynamics*, **9** (8), 391–409.

Huck, T., O. Arzel, and F. Sévellec, 2015: Multidecadal variability of the overturning circulation in presence of eddy turbulence. *Journal of Physical Oceanography*, **45** (1), 157–173.

Huck, T., A. Colin de Verdière, and A. J. Weaver, 1999: Interdecadal variability of the thermohaline circulation in box-ocean models forced by fixed surface fluxes. *Journal of physical oceanography*, **29** (5), 865–892.

Huck, T., and G. K. Vallis, 2001: Linear stability analysis of the three-dimensional thermally-driven ocean circulation: application to interdecadal oscillations. *Tellus A*, **53** (4), 526–545.

Huck, T., G. K. Vallis, and A. Colin de Verdière, 2001: On the robustness of the interdecadal modes of the thermohaline circulation. *Journal of climate*, **14** (5), 940–963.

691 Hughes, G. O., A. M. C. Hogg, and R. W. Griffiths, 2009: Available potential energy and irre-
 692 versible mixing in the meridional overturning circulation. *Journal of Physical Oceanography*,
 693 **39 (12)**, 3130–3146.

694 Jamet, Q., W. Dewar, N. Wienders, and B. Deremble, 2019: Spatiotemporal patterns of chaos in
 695 the atlantic overturning circulation. *Geophysical Research Letters*, **46 (13)**, 7509–7517.

696 Jamet, Q., T. Huck, O. Arzel, J.-M. Campin, and A. C. de Verdière, 2016: Oceanic control of
 697 multidecadal variability in an idealized coupled GCM. *Climate Dynamics*, **46 (9-10)**, 3079–
 698 3095, doi:10.1007/s00382-015-2754-3.

699 Kerr, R. A., 2000: A north atlantic climate pacemaker for the centuries. *Science*, **288 (5473)**,
 700 1984–1985.

701 Klocker, A., and T. J. McDougall, 2010: Influence of the nonlinear equation of state on global
 702 estimates of diapycnal advection and diffusion. *Journal of Physical Oceanography*, **40 (8)**,
 703 1690–1709.

704 Kushnir, Y., 1994: Interdecadal variations in North Atlantic sea surface temperature and associated
 705 atmospheric conditions. *Journal of Climate*, **7 (1)**, 141–157.

706 Leroux, S., T. Penduff, L. Bessières, J.-M. Molines, J.-M. Brankart, G. Sérazin, B. Barnier, and
 707 L. Terray, 2018: Intrinsic and atmospherically forced variability of the amoc: Insights from a
 708 large-ensemble ocean hindcast. *Journal of Climate*, **31 (3)**, 1183–1203.

709 Levitus, S., and Coauthors, 2012: World ocean heat content and thermosteric sea level change
 710 (0–2000 m), 1955–2010. *Geophysical Research Letters*, **39 (10)**.

711 Lorenz, E. N., 1955: Available potential energy and the maintenance of the general circulation.
 712 *Tellus*, **7 (2)**, 157–167.

713 Marshall, J., A. Adcroft, C. Hill, L. Perelman, and C. Heisey, 1997: A finite-volume, incompress-
714 ible Navier Stokes model for studies of the ocean on parallel computers. *Journal of Geophysical*
715 *Research: Oceans*, **102 (C3)**, 5753–5766.

716 Martin, P. E., B. K. Arbic, A. McC. Hogg, A. E. Kiss, J. R. Munroe, and J. R. Blundell, 2020:
717 Frequency-domain analysis of the energy budget in an idealized coupled ocean–atmosphere
718 model. *Journal of Climate*, **33 (2)**, 707–726.

719 Muir, L. C., and A. V. Fedorov, 2017: Evidence of the amoc interdecadal mode related to westward
720 propagation of temperature anomalies in cmip5 models. *Climate Dynamics*, **48 (5-6)**, 1517–
721 1535.

722 Nikurashin, M., and G. Vallis, 2011: A theory of deep stratification and overturning circulation in
723 the ocean. *Journal of Physical Oceanography*, **41 (3)**, 485–502.

724 Nikurashin, M., and G. Vallis, 2012: A theory of the interhemispheric meridional overturning
725 circulation and associated stratification. *Journal of Physical Oceanography*, **42 (10)**, 1652–
726 1667.

727 Nycander, J., M. Hieronymus, and F. Roquet, 2015: The nonlinear equation of state of sea water
728 and the global water mass distribution. *Geophysical Research Letters*, **42 (18)**, 7714–7721.

729 Ortega, P., J. Mignot, D. Swingedouw, F. Sévellec, and E. Guilyardi, 2015: Reconciling two alter-
730 native mechanisms behind bi-decadal variability in the North Atlantic. *Progress in Oceanogra-*
731 *phy*, **137**, 237–249.

732 Penduff, T., M. Juza, B. Barnier, J. Zika, W. K. Dewar, A.-M. Treguier, J.-M. Molines, and N. Au-
733 diffren, 2011: Sea level expression of intrinsic and forced ocean variabilities at interannual time
734 scales. *Journal of Climate*, **24 (21)**, 5652–5670.

735 Reguero, B. G., I. J. Losada, and F. J. Méndez, 2019: A recent increase in global wave power as a
736 consequence of oceanic warming. *Nature communications*, **10** (1), 1–14.

737 Saenz, J. A., R. Tailleux, E. D. Butler, G. O. Hughes, and K. I. Oliver, 2015: Estimating Lorenz’s
738 reference state in an ocean with a nonlinear equation of state for seawater. *Journal of Physical*
739 *Oceanography*, **45** (5), 1242–1257.

740 Schlesinger, M. E., and N. Ramankutty, 1994: An oscillation in the global climate system of period
741 65–70 years. *Nature*, **367** (6465), 723–726.

742 Scotti, A., and B. White, 2014: Diagnosing mixing in stratified turbulent flows with a locally
743 defined available potential energy. *Journal of Fluid Mechanics*, **740**, 114–135.

744 Sévellec, F., A. C. N. Garabato, and T. Huck, 2020: Damping of climate-scale oceanic
745 variability by mesoscale eddy turbulence. *Journal of Physical Oceanography*, doi:10.1175/
746 JPO-D-20-0141.1, URL <https://journals.ametsoc.org/view/journals/phoc/aop/JPO-D-20-0141.1/JPO-D-20-0141.1.xml>.

747

748 Sohail, T., B. Gayen, and A. M. Hogg, 2018: Convection enhances mixing in the southern ocean.
749 *Geophysical Research Letters*, **45** (9), 4198–4207.

750 Spall, M. A., 2008: Low-frequency interaction between horizontal and overturning gyres in the
751 ocean. *Geophysical Research Letters*, **35** (18), doi:<https://doi.org/10.1029/2008GL035206>.

752 Stammer, D., 1997: Global characteristics of ocean variability estimated from regional
753 TOPEX/POSEIDON altimeter measurements. *Journal of Physical Oceanography*, **27** (8),
754 1743–1769.

755 Sutton, R. T., G. D. McCarthy, J. Robson, B. Sinha, A. T. Archibald, and L. J. Gray, 2018: Atlantic
 756 multidecadal variability and the UK ACSIS program. *Bulletin of the American Meteorological*
 757 *Society*, **99** (2), 415–425.

758 Sérazin, G., T. Penduff, B. Barnier, J.-M. Molines, B. K. Arbic, M. Müller, and L. Terray, 2018:
 759 Inverse Cascades of Kinetic Energy as a Source of Intrinsic Variability: A Global OGCM Study.
 760 *Journal of Physical Oceanography*, **48** (6), 1385–1408.

761 Sérazin, G., T. Penduff, S. Grégorio, B. Barnier, J.-M. Molines, and L. Terray, 2015: Intrinsic vari-
 762 ability of sea level from global ocean simulations: Spatiotemporal scales. *Journal of Climate*,
 763 **28** (10), 4279–4292.

764 Sévellec, F., and A. V. Fedorov, 2013: The leading, interdecadal eigenmode of the Atlantic merid-
 765 ional overturning circulation in a realistic ocean model. *Journal of Climate*, **26** (7), 2160–2183.

766 Tailleux, R., 2009: On the energetics of stratified turbulent mixing, irreversible thermodynamics,
 767 Boussinesq models and the ocean heat engine controversy. *Journal of Fluid Mechanics*, **638**,
 768 339–382.

769 Te Raa, L. A., and H. A. Dijkstra, 2002: Instability of the thermohaline ocean circulation on
 770 interdecadal timescales. *Journal of physical oceanography*, **32** (1), 138–160.

771 Toggweiler, J. R., and B. Samuels, 1998: On the ocean’s large-scale circulation near the limit of
 772 no vertical mixing. *Journal of Physical Oceanography*, **28** (9), 1832–1852.

773 Vallis, G. K., 2017: *Atmospheric and oceanic fluid dynamics*. Cambridge University Press.

774 Von Storch, H., and F. W. Zwiers, 2001: *Statistical analysis in climate research*. Cambridge uni-
 775 versity press.

776 Winters, K. B., P. N. Lombard, J. J. Riley, and E. A. D’Asaro, 1995: Available potential energy
777 and mixing in density-stratified fluids. *Journal of Fluid Mechanics*, **289**, 115–128.

778 Winton, M., 1997: The damping effect of bottom topography on internal decadal-scale oscillations
779 of the thermohaline circulation. *Journal of physical oceanography*, **27** (1), 203–208.

780 Zemskova, V. E., B. L. White, and A. Scotti, 2015: Available potential energy and the general
781 circulation: Partitioning wind, buoyancy forcing, and diapycnal mixing. *Journal of Physical*
782 *Oceanography*, **45** (6), 1510–1531.

783 Zemskova, V. E., B. L. White, and A. Scotti, 2021: Energetics of a rotating wind-forced horizontal
784 convection model of a reentrant channel. *Journal of Physical Oceanography*, **51** (7), 2271–2290.

785 Zhang, R., R. Sutton, G. Danabasoglu, T. L. Delworth, W. M. Kim, J. Robson, and S. G. Yeager,
786 2016: Comment on “The Atlantic Multidecadal Oscillation without a role for ocean circulation”.
787 *Science*, **352** (6293), 1527–1527.

788 Zhang, R., R. Sutton, G. Danabasoglu, Y.-O. Kwon, R. Marsh, S. G. Yeager, D. E. Amrhein, and
789 C. M. Little, 2019: A review of the role of the Atlantic Meridional Overturning Circulation in
790 Atlantic multidecadal variability and associated climate impacts. *Reviews of Geophysics*, **57** (2),
791 316–375.

| | | |
|-----|---|----|
| 792 | LIST OF TABLES | |
| 793 | Table 1. List of all terms in the energy budget shown in figure 3 | 42 |
| 794 | Table 2. Transfer values for all terms in the energy budget for the no wind ($\tau_0 =$ | |
| 795 | 0Nm^{-2}), intermediate wind $\tau_0 = (0.05\text{Nm}^{-2})$ and climatological wind ($\tau_0 =$ | |
| 796 | 0.1Nm^{-2}) experiments. | 43 |

| KE and APE Dissipation | |
|--------------------------------------|--|
| $D_{KE^{LF}}$ | $\rho_0 \int_V \overline{(u^{LF} V_u^{LF} + v^{LF} V_v^{LF})} dV$ |
| $D_{KE^{MEAN}}$ | $\rho_0 \int_V (\bar{u} \bar{V}_u + \bar{v} \bar{V}_v) dV$ |
| $D_{KE^{HF}}$ | $-F_{KE^{MEAN}} - C(APE, KE) - D_{KE^{LF}} - D_{KE^{MEAN}}$ |
| $D_{APE^{LF}}$ | $-\int_V g z_r(\rho, t) \overline{D^{LF}} dV$ |
| $D_{APE^{MEAN}}$ | $\int_V g z \bar{D} dV - \int_V g z_r(\rho, t) \bar{D} dV$ |
| $D_{APE^{HF}}$ | $-F_{APE^{MEAN}} - D_{APE^{LF}} - D_{APE^{MEAN}} + C(APE, KE)$ |
| KE and APE Forcing | |
| $F_{KE^{MEAN}}$ | $\rho_0 \int_V \bar{u} \bar{F}_u dV$ |
| $F_{APE^{MEAN}}$ | $-\int_V g z_r(\rho) \bar{F} dV$ |
| Conversion between reservoirs | |
| $C(KE^{LF}, KE^{HF})$ | $C(APE^{LF}, KE^{LF}) + C(KE^{MEAN}, KE^{LF}) + D_{KE^{LF}}$ |
| $C(KE^{MEAN}, KE^{LF})$ | $\rho_0 \int_V \left(\bar{u} \nabla \cdot (\mathbf{v}^{LF} u^{LF}) + \bar{v} \nabla \cdot (\mathbf{v}^{LF} v^{LF}) \right) dV$ |
| $C(KE^{MEAN}, KE^{HF})$ | $F_{KE^{MEAN}} + C(APE^{MEAN}, KE^{MEAN}) + D_{KE^{MEAN}} - C(KE^{MEAN}, KE^{LF})$ |
| $C(APE^{LF}, APE^{HF})$ | $-C(APE^{LF}, KE^{LF}) + C(APE^{MEAN}, APE^{LF}) + D_{APE^{LF}}$ |
| $C(APE^{MEAN}, APE^{LF})$ | $-\int_V g \bar{\rho}^{LF} \bar{w}^{LF} dV - g \int_V \overline{z_r(\rho, t) \mathbf{v}^{LF} \cdot \nabla \rho^{LF}} - \overline{z_r(\rho, t) \bar{\mathbf{v}} \cdot \nabla \rho^{LF}} dV$ |
| $C(APE^{MEAN}, APE^{HF})$ | $-C(APE^{MEAN}, APE^{LF}) - C(APE^{MEAN}, KE^{MEAN}) + D_{APE^{MEAN}} + F_{APE^{MEAN}}$ |
| $C(APE^{MEAN}, KE^{MEAN})$ | $-\int_V g \bar{\rho} \bar{w} dV$ |
| $C(APE^{LF}, KE^{LF})$ | $-\int_V g \bar{\rho}^{LF} \bar{w}^{LF} dV$ |
| $C(APE^{HF}, KE^{HF})$ | $C(APE, KE) - C(APE^{MEAN}, KE^{LF}) - C(APE^{MEAN}, KE^{MEAN})$ |
| $C(APE, KE)$ | $\int_V g z \bar{\nabla} \bar{\mathbf{v}} \bar{\rho} dV$ |

TABLE 1. List of all terms in the energy budget shown in figure 3

| | $\tau_0 = 0 \text{ N m}^{-2}$ | $\tau_0 = 0.05 \text{ N m}^{-2}$ | $\tau_0 = 0.1 \text{ N m}^{-2}$ |
|--------------------------------------|-------------------------------|----------------------------------|---------------------------------|
| KE and APE Dissipation | | | |
| $D_{KE^{LF}}$ | -5 GW | -3 GW | -2 GW |
| $D_{KE^{MEAN}}$ | -5 GW | -8 GW | -15 GW |
| $D_{KE^{HF}}$ | -22 GW | -22 GW | -36 GW |
| $D_{APE^{LF}}$ | -16 GW | -7 GW | -5 GW |
| $D_{APE^{MEAN}}$ | -18 GW | -30 GW | -42 GW |
| $D_{APE^{HF}}$ | -53 GW | -56 GW | -62 GW |
| KE and APE Forcing | | | |
| $F_{KE^{MEAN}}$ | 0 GW | 7 GW | 34 GW |
| $F_{APE^{MEAN}}$ | 119 GW | 119 GW | 128 GW |
| Conversion between reservoirs | | | |
| $C(KE^{LF}, KE^{HF})$ | 0 GW | 0 GW | -1 GW |
| $C(KE^{MEAN}, KE^{LF})$ | 1 GW | 1 GW | 0 GW |
| $C(KE^{MEAN}, KE^{HF})$ | 2 GW | 3 GW | 8 GW |
| $C(APE^{LF}, APE^{HF})$ | 29 GW | 14 GW | 7 GW |
| $C(APE^{MEAN}, APE^{LF})$ | 49 GW | 23 GW | 13 GW |
| $C(APE^{MEAN}, APE^{HF})$ | 44 GW | 61 GW | 84 GW |
| $C(APE^{MEAN}, KE^{MEAN})$ | 8 GW | 5 GW | -11 GW |
| $C(APE^{LF}, KE^{LF})$ | 4 GW | 2 GW | 1 GW |
| $C(APE^{HF}, KE^{HF})$ | 20 GW | 19 GW | 29 GW |
| $C(APE, KE)$ | 32 GW | 26 GW | 19 GW |

TABLE 2. Transfer values for all terms in the energy budget for the no wind ($\tau_0 = 0 \text{ N m}^{-2}$), intermediate wind

$\tau_0 = (0.05 \text{ N m}^{-2})$ and climatological wind ($\tau_0 = 0.1 \text{ N m}^{-2}$) experiments.

LIST OF FIGURES

- Fig. 1.** Schematic showing how the reference depth z_r associated with a given density ρ is calculated. Left: meridional section of the physical space where volume V_1 (coloured in red) above the isopycnal $\rho = \text{const.}$ is shown. Right: adiabatic rearrangement where the previous isopycnal is horizontal with the same volume of water V_1 above it. $z_r(\rho)$ is the depth of this isopycnal after the rearrangement. 46
- Fig. 2.** Time evolution (in years) of the reference depth (in m) of several isotherms (in $^{\circ}\text{C}$) in the experiment without wind forcing. 47
- Fig. 3.** Schematic view of the transfer between the different reservoirs of LF, HF and mean APE and KE, and BPE. KE dissipation is in blue, KE forcing is in red, transfers between reservoirs are in orange, BPE/APE transfer due to forcing and parametrized diffusion are in pink and green, respectively. Names of all transfers are indicated near the corresponding arrow and summarized in table (1). 48
- Fig. 4.** Analytical zonal wind stress as a function of latitude for $\tau_0 = 0 \text{ Nm}^{-2}$ (blue line), $\tau_0 = 0.05 \text{ Nm}^{-2}$ (orange line) and $\tau_0 = 0.1 \text{ Nm}^{-2}$ (green line). 49
- Fig. 5.** Volume average of the temperature spectrum as a function of frequency calculated from 5 days (orange line) and 50 days (blue line) average outputs for $\tau_0 = 0 \text{ Nm}^{-2}$ (top left panel), 0.05 Nm^{-2} (top right panel) and 0.1 Nm^{-2} (bottom panel). The black vertical lines on each panel show the peak magnitude for each experiment and the red vertical lines show the LF/HF 3.5 year separation. 50
- Fig. 6.** First Complex EOF calculated on 1 year averaged 3D temperature outputs ($^{\circ}\text{C}$) of the $\tau_0 = 0 \text{ Nm}^{-2}$ run, accounting for 60% of the variability. Top left: real part of the SST, top right imaginary part of the SST. Middle left: CEOF real part along the meridional section (longitude = 800 km) shown by a red line on the top left and right panels, middle right: imaginary part along the same section. Black contours show isotherms of the time mean temperature. Bottom: real (red solid) and imaginary (red dotted) part of the principal component of the first CEOF. The blue line shows the time evolution of the APE (in EJ). 51
- Fig. 7.** Left column: Sea Surface height standard deviation (m) calculated from 50 days average and time mean (black contours), middle column: vertical integral of the time mean LF density variance ($\text{kg}^2 \text{ m}^{-5}$), right column: time mean of the vertical integral of the LF APE (J m^{-2}). $\tau_0 = 0 \text{ Nm}^{-2}$, 0.05 Nm^{-2} and 0.1 Nm^{-2} are respectively shown on the first, second and third line. Note that the colorscale is different for each figure. 52
- Fig. 8.** Same as in Figure 6 but for an intermediate double gyre wind forcing of $\tau_0 = 0.05 \text{ Nm}^{-2}$. The leading CEOF accounts for 28% of the temperature variance. The red line on the two top figures shows the same meridional section as in Fig. 6 used to plot the two figures in the middle. 53
- Fig. 9.** Same as in Figure 6 but for a climatological double gyre wind forcing of $\tau_0 = 0.1 \text{ Nm}^{-2}$. The leading CEOF accounts for 7% of the temperature variance. 54
- Fig. 10.** Schematic showing the Exchange of Energy between the different reservoirs (shown by black boxes) for the $\tau_0 = 0 \text{ Nm}^{-2}$ run. The conversion from BPE to APE forcing achieved by surface heat fluxes is shown by green arrows, the conversion of APE to BPE because of diffusive fluxes are shown in pink. Dissipation of KE by viscous forces is shown by blue arrows and the conversion between the different reservoirs by orange arrows. The direction

of the conversion follows the arrow direction. Conversions are expressed in $\text{GW} = 10^9 \text{W}$,
the KE in $\text{PJ} = 10^{15} \text{J}$ and the APE in $\text{EJ} = 10^{18} \text{J}$ 55

Fig. 11. Vertical integral of the conversion between mean APE and HF APE (first column)
 $C(APE^{MEAN}, APE^{HF})$, mean APE and LF APE $C(APE^{MEAN}, APE^{LF})$ (second column).
Unit is in GW. The third column shows the vertical integral of the density variance transfer
from mean to LF (units: $\text{kg}^2 \text{m}^{-6} \text{s}^{-1}$). Note that the colorbar differs between the different
rows. The last column shows the mean APE forcing (or transfer from BPE to mean APE
due to heat fluxes) (unit GW). The first, second, and third line show respectively the three
conversion term for the three wind intensity $\tau_0 = 0 \text{ N/m}^2$, $\tau_0 = 0.05 \text{ N/m}^2$ and $\tau_0 = 0.1$
 N/m^2 . $C(APE^{LF}, APE^{HF})$ is not shown but look very similar to $C(APE^{MEAN}, APE^{LF})$ 56

Fig. 12. Same as figure 10 but with an intermediate double gyre wind stress surface forcing of $\tau_0 =$
 0.05 N m^{-2} . The KE forcing made by the wind stress is shown with a red arrow. 57

Fig. 13. Same as figure 10 but with a double gyre wind stress surface forcing of $\tau_0 = 0.1 \text{ N m}^{-2}$. The
KE forcing made by the wind stress is shown with a red arrow. 58

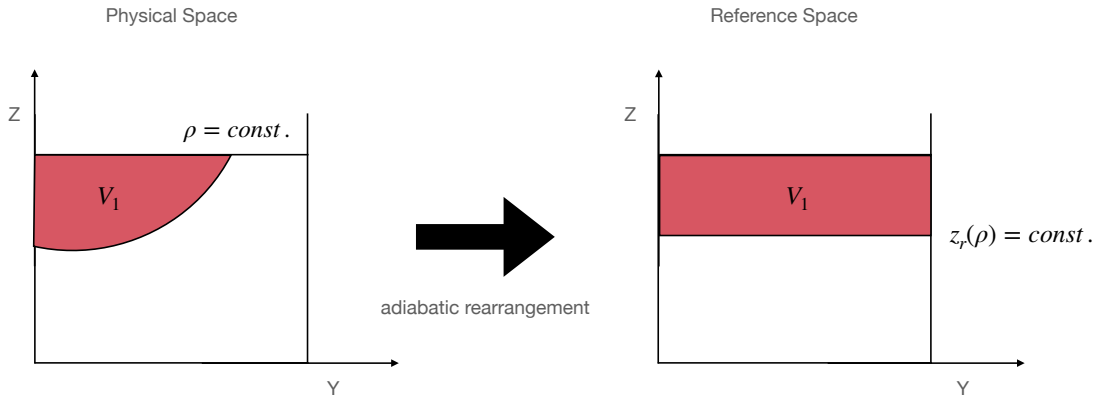
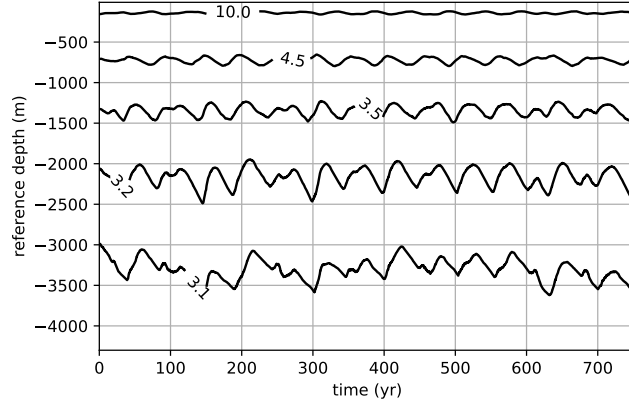


FIG. 1. Schematic showing how the reference depth z_r associated with a given density ρ is calculated. Left: meridional section of the physical space where volume V_1 (coloured in red) above the isopycnal $\rho = \text{const.}$ is shown. Right: adiabatic rearrangement where the previous isopycnal is horizontal with the same volume of water V_1 above it. $z_r(\rho)$ is the depth of this isopycnal after the rearrangement.



860 FIG. 2. Time evolution (in years) of the reference depth (in m) of several isotherms (in $^{\circ}\text{C}$) in the experiment
 861 without wind forcing.

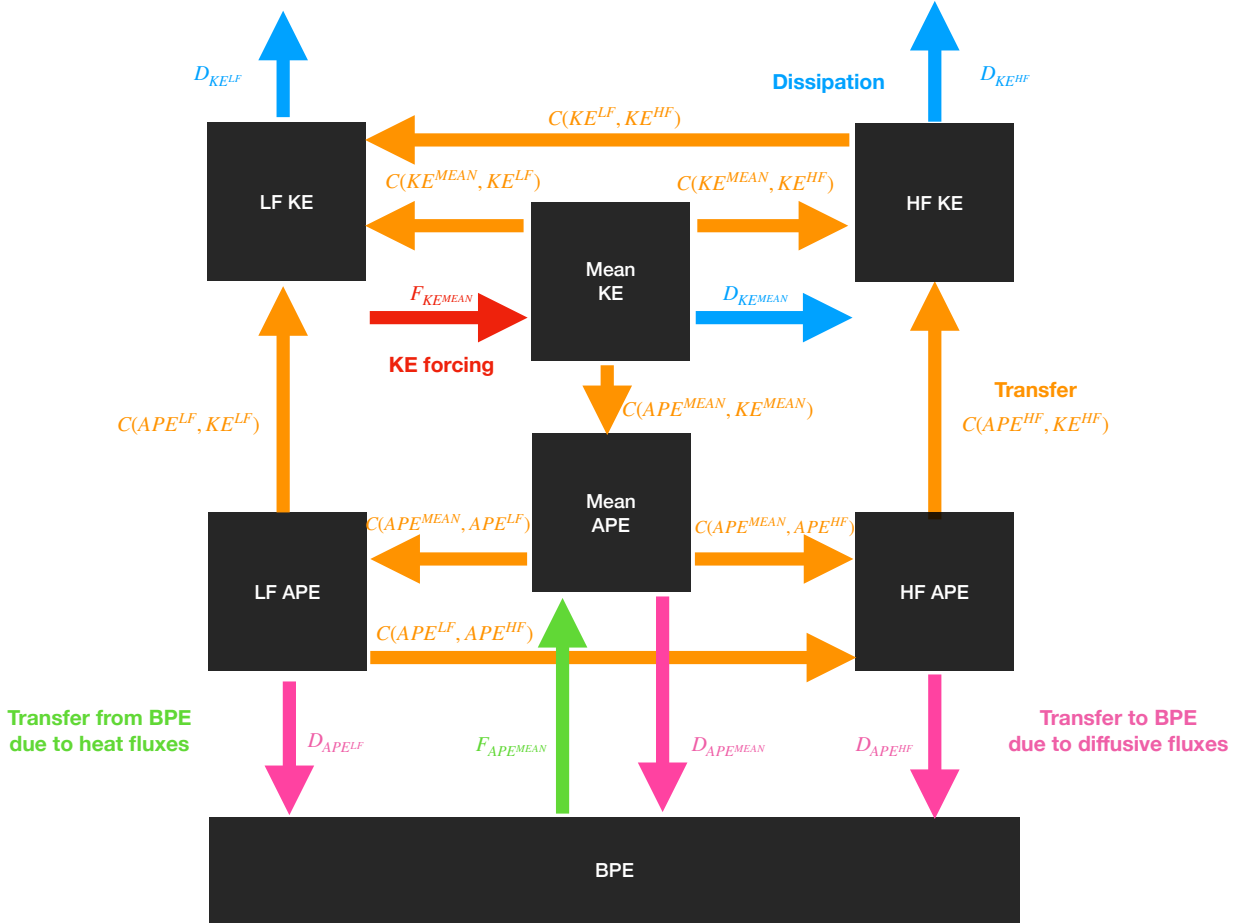
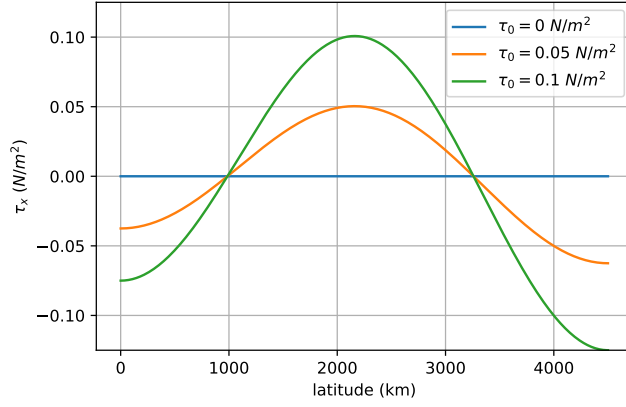


FIG. 3. Schematic view of the transfer between the different reservoirs of LF, HF and mean APE and KE, and BPE. KE dissipation is in blue, KE forcing is in red, transfers between reservoirs are in orange, BPE/APE transfer due to forcing and parametrized diffusion are in pink and green, respectively. Names of all transfers are indicated near the corresponding arrow and summarized in table (1).



866 FIG. 4. Analytical zonal wind stress as a function of latitude for $\tau_0 = 0 \text{ Nm}^{-2}$ (blue line), $\tau_0 = 0.05 \text{ Nm}^{-2}$
867 (orange line) and $\tau_0 = 0.1 \text{ Nm}^{-2}$ (green line).

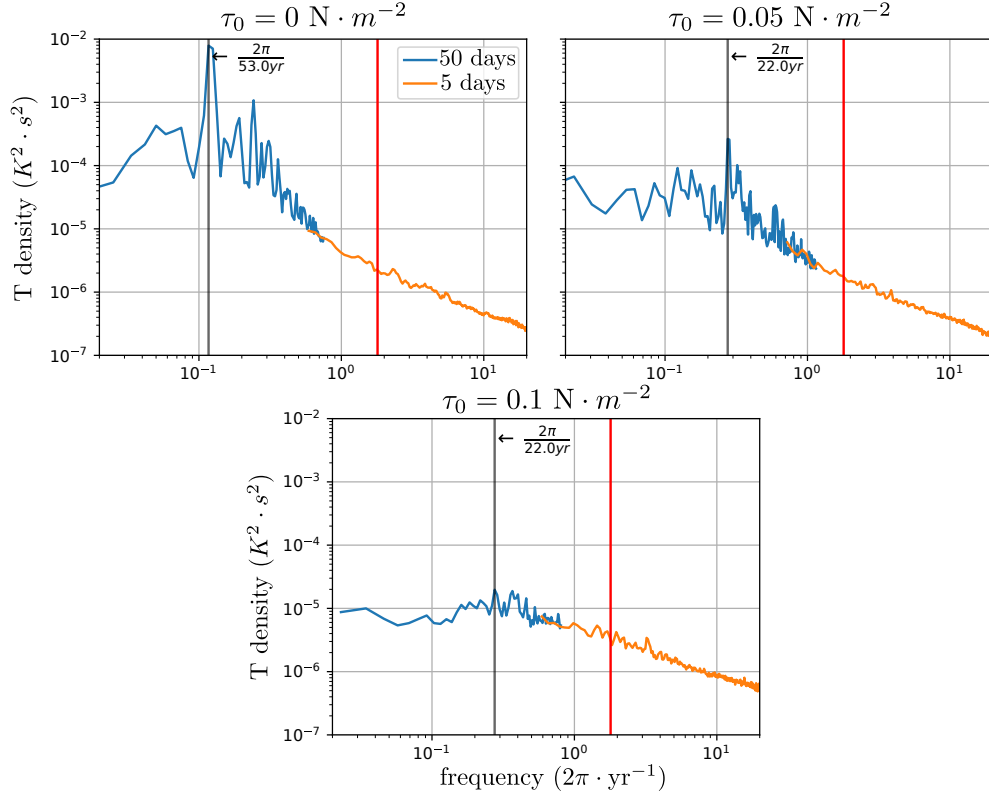
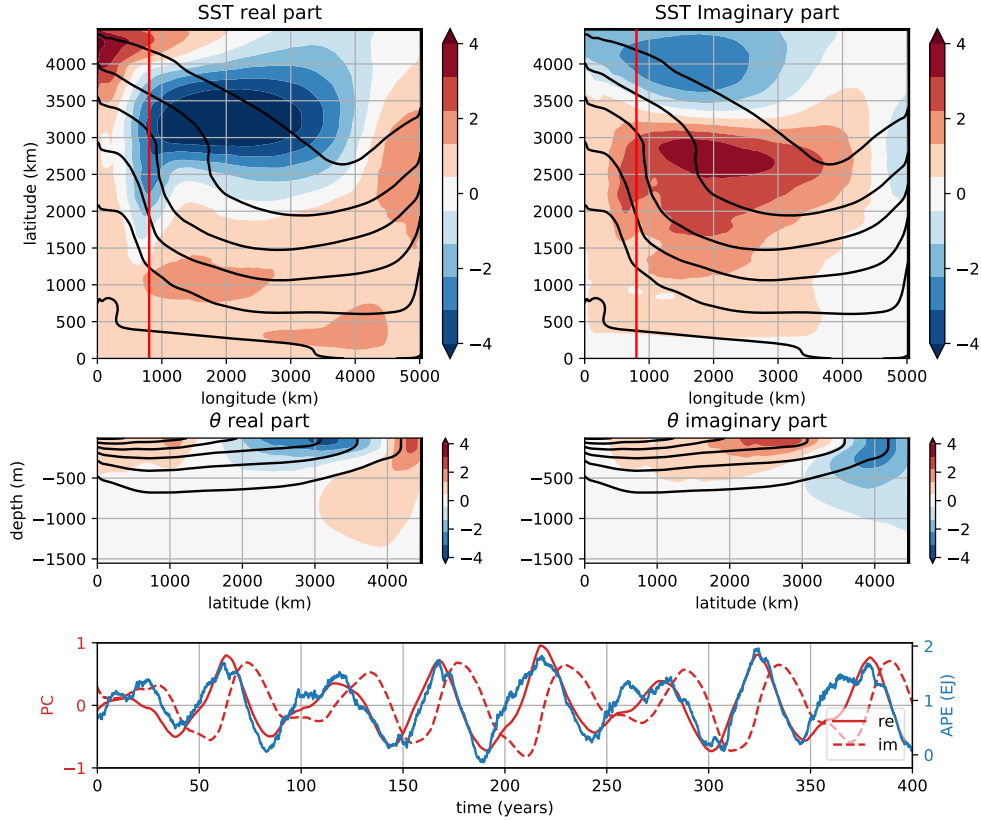


FIG. 5. Volume average of the temperature spectrum as a function of frequency calculated from 5 days (orange line) and 50 days (blue line) average outputs for $\tau_0 = 0 \text{ N m}^{-2}$ (top left panel), 0.05 N m^{-2} (top right panel) and 0.1 N m^{-2} (bottom panel). The black vertical lines on each panel show the peak magnitude for each experiment and the red vertical lines show the LF/HF 3.5 year separation.



872 FIG. 6. First Complex EOF calculated on 1 year averaged 3D temperature outputs ($^{\circ}\text{C}$) of the $\tau_0 = 0 \text{ Nm}^{-2}$
 873 run, accounting for 60% of the variability. Top left: real part of the SST, top right imaginary part of the SST.
 874 Middle left: CEOF real part along the meridional section (longitude = 800 km) shown by a red line on the top
 875 left and right panels, middle right: imaginary part along the same section. Black contours show isotherms of the
 876 time mean temperature. Bottom: real (red solid) and imaginary (red dotted) part of the principal component of
 877 the first CEOF. The blue line shows the time evolution of the APE (in EJ).

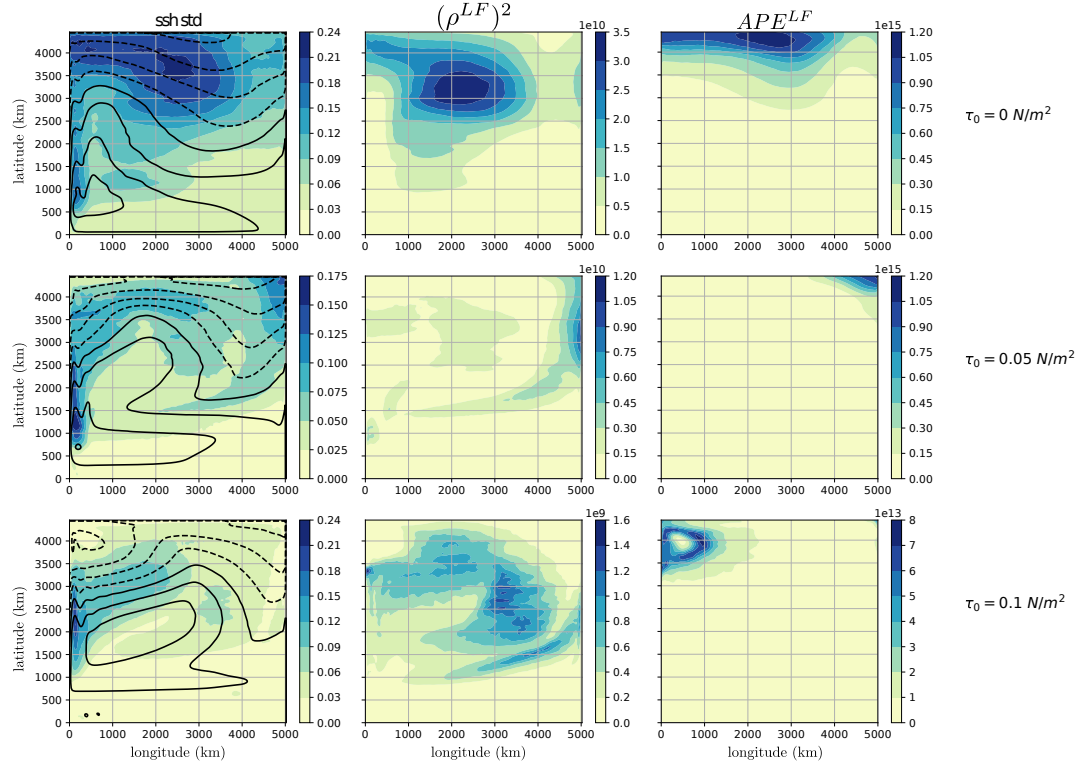


FIG. 7. Left column: Sea Surface height standard deviation (m) calculated from 50 days average and time mean (black contours), middle column: vertical integral of the time mean LF density variance ($\text{kg}^2 \text{m}^{-5}$), right column: time mean of the vertical integral of the LF APE (Jm^{-2}). $\tau_0 = 0 \text{ Nm}^{-2}$, 0.05 Nm^{-2} and 0.1 Nm^{-2} are respectively shown on the first, second and third line. Note that the colorscale is different for each figure.

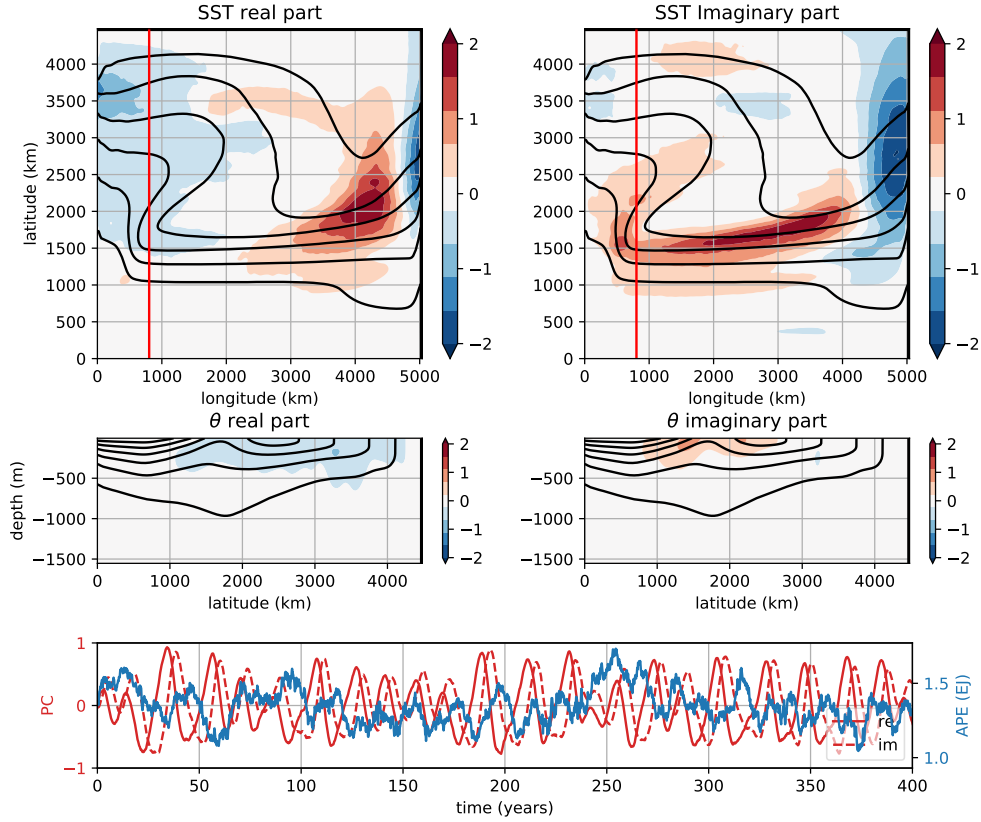
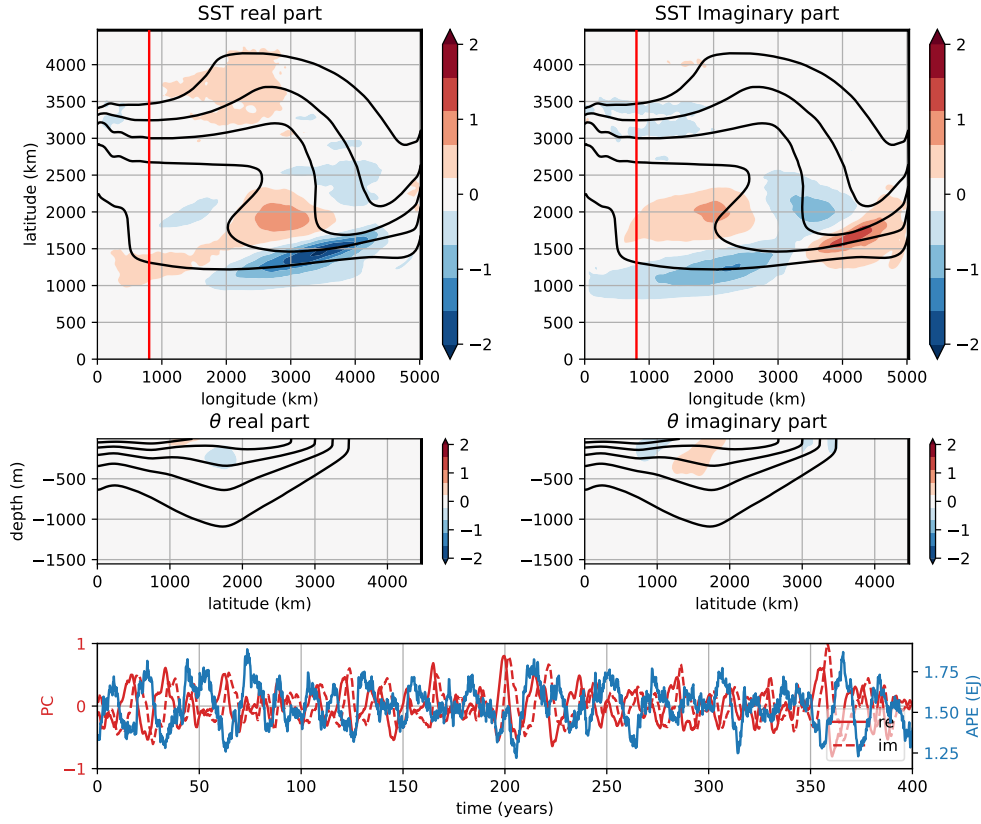


FIG. 8. Same as in Figure 6 but for an intermediate double gyre wind forcing of $\tau_0 = 0.05 \text{ N m}^{-2}$. The leading CEOF accounts for 28% of the temperature variance. The red line on the two top figures shows the same meridional section as in Fig. 6 used to plot the two figures in the middle.



885 FIG. 9. Same as in Figure 6 but for a climatological double gyre wind forcing of $\tau_0 = 0.1 \text{ N m}^{-2}$. The leading
886 CEOF accounts for 7% of the temperature variance.

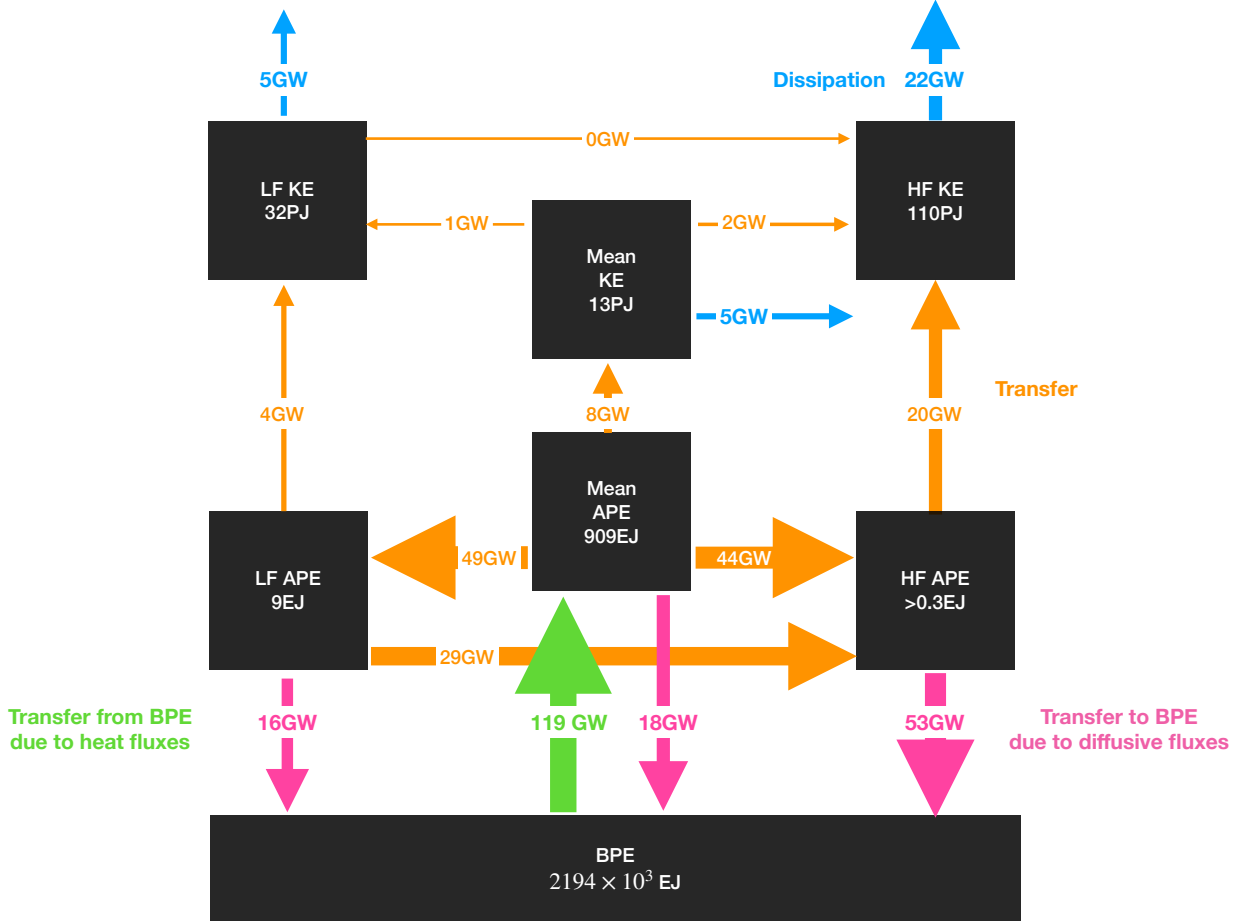


FIG. 10. Schematic showing the Exchange of Energy between the different reservoirs (shown by black boxes) for the $\tau_0 = 0 \text{ Nm}^{-2}$ run. The conversion from BPE to APE forcing achieved by surface heat fluxes is shown by green arrows, the conversion of APE to BPE because of diffusive fluxes are shown in pink. Dissipation of KE by viscous forces is shown by blue arrows and the conversion between the different reservoirs by orange arrows. The direction of the conversion follows the arrow direction. Conversions are expressed in $\text{GW} = 10^9 \text{ W}$, the KE in $\text{PJ} = 10^{15} \text{ J}$ and the APE in $\text{EJ} = 10^{18} \text{ J}$.

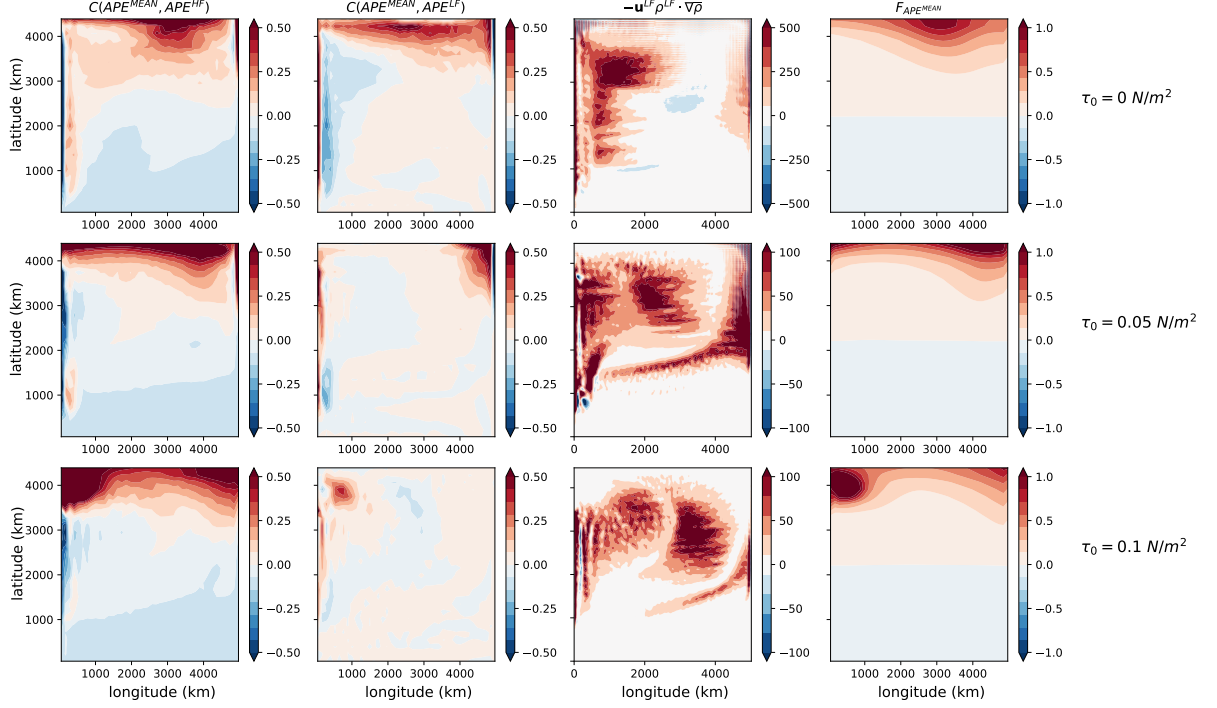


FIG. 11. Vertical integral of the conversion between mean APE and HF APE (first column) $C(APE^{MEAN}, APE^{HF})$, mean APE and LF APE $C(APE^{MEAN}, APE^{LF})$ (second column). Unit is in GW. The third column shows the vertical integral of the density variance transfer from mean to LF (units: $\text{kg}^2 \text{ m}^{-6} \text{ s}^{-1}$). Note that the colorbar differs between the different rows. The last column shows the mean APE forcing (or transfer from BPE to mean APE due to heat fluxes) (unit GW). The first, second, and third line show respectively the three conversion term for the three wind intensity $\tau_0 = 0 \text{ N/m}^2$, $\tau_0 = 0.05 \text{ N/m}^2$ and $\tau_0 = 0.1 \text{ N/m}^2$. $C(APE^{LF}, APE^{HF})$ is not shown but look very similar to $C(APE^{MEAN}, APE^{LF})$.

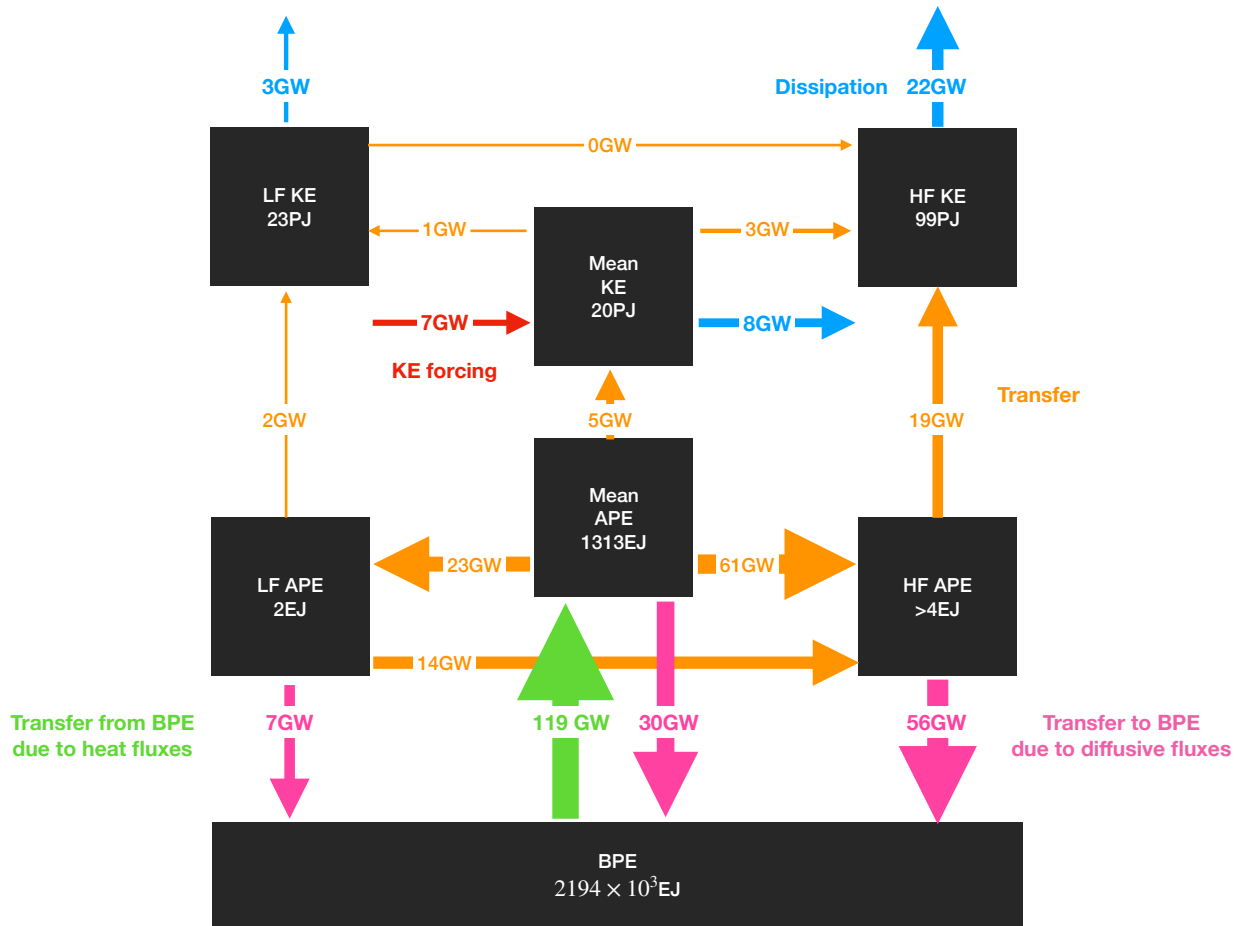


FIG. 12. Same as figure 10 but with an intermediate double gyre wind stress surface forcing of $\tau_0 = 0.05 \text{ N m}^{-2}$. The KE forcing made by the wind stress is shown with a red arrow.

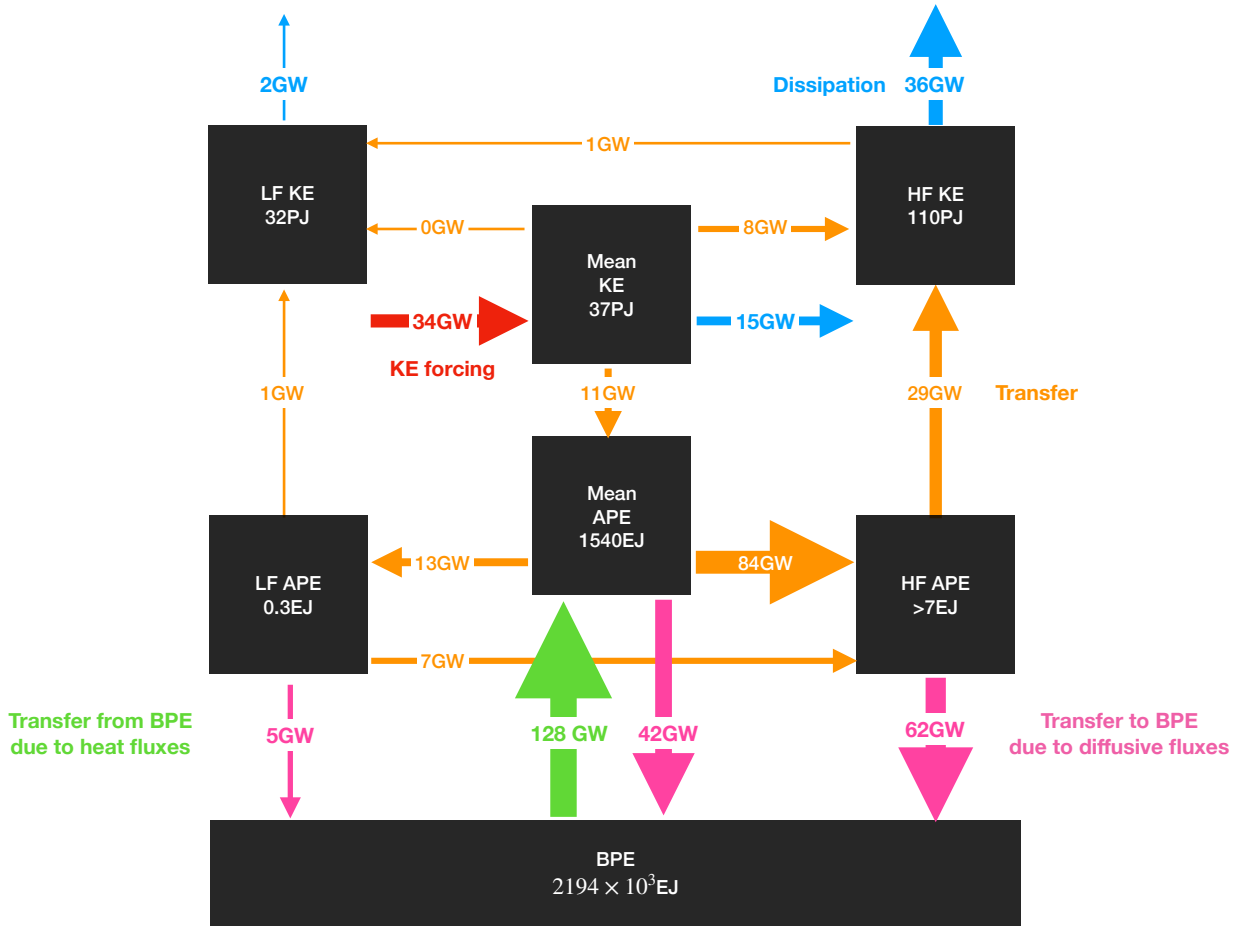


FIG. 13. Same as figure 10 but with a double gyre wind stress surface forcing of $\tau_0 = 0.1 \text{ N m}^{-2}$. The KE forcing made by the wind stress is shown with a red arrow.